University of South Florida
Scholar Commons

Graduate Theses and Dissertations | Graduate School

11-6-2008

Irradiated Single Crystal 3C-SiC as a Maximum Temperature Sensor

Viacheslav G. Kuryachiy
University of South Florida

Follow this and additional works at: https://scholarcommons.usf.edu/etd

Part of the American Studies Commons

Scholar Commons Citation
Kuryachiy, Viacheslav G., "Irradiated Single Crystal 3C-SiC as a Maximum Temperature Sensor" (2008). *Graduate Theses and Dissertations.*
https://scholarcommons.usf.edu/etd/351

This Thesis is brought to you for free and open access by the Graduate School at Scholar Commons. It has been accepted for inclusion in Graduate Theses and Dissertations by an authorized administrator of Scholar Commons. For more information, please contact scholarcommons@usf.edu.

www.manaraa.com

Irradiated Single Crystal 3C-SiC as a Maximum Temperature Sensor

by

Viacheslav G. Kuryachiy

A thesis submitted in partial fulfillment
of the requirements for the degree of
Master of Science in Mechanical Engineering
Department of Mechanical Engineering
College of Engineering
University of South Florida

Major Professor: Alex Volinsky, Ph.D.
Craig Lusk, Ph.D.
Jose Porteiro, Ph.D.

Date of Approval:
November 6, 2008

Keywords: neutron irradiation, x-ray diffraction, lattice parameter, point defects, thermal annealing

© Copyright 2008 , Viacheslav G. Kuryachiy

المنارة للاستشارات

www.manaraa.com

Acknowledgements

First of all, I would like to thank my advisor Dr. Alex Volinsky for assistance through the entire process of my research and thesis preparation. I am grateful to him as well as to the University of South Florida for giving me such a great opportunity to study, work and earn my Master's Degree. I would also like to thank the faculty of the Mechanical Engineering Department for all the knowledge I have gained, namely to Dr. Porteiro, Dr. Dubey, Dr. Lusk and Dr. Rahman. In addition, my gratitude is to the staff of the ME department, specifically to Sue Britten for being patient and kind throughout my entire stay at USF.

المنارة للاستشارات

www.manaraa.com

Table of Contents

List of Tables iv

List of Figures v

List of Nomenclature viii

ABSTRACT xi

Chapter 1. Introduction 1

1.2 Statement of work 2

1.3 Hard to access parts temperature measurement tools 3

Chapter 2. The Maximum Temperature Crystal Sensor 7

2.1 Material selection for MTCS 7

2.2 Technical characteristics of MTCS 8

2.3 Manufacturing of MTCS 10

2.4 MTCS design and installation techniques 13

Chapter 3. Neutron Irradiation of Silicon Carbide 17

3.1 Features of neutron irradiation of materials 17

3.2 Principle of neutron irradiation 17

3.3 Atoms displacement energy of irradiated 3C-SiC 19

3.4 Volume change of 3C-SiC due to neutron irradiation 20

3.5 Point defects in 3C-SiC 24

3.6 Defects concentration in 3C-SiC 26

3.7 Annealing temperature of irradiated 3C-SiC 28

المنارة للاستشارات
www.manaraa.com

Chapter 4. Diffraction Analysis 30
4.1 Diffractometer method 30
4.2 Application of Bragg's law 31
4.3 Lorenz factor 35

Chapter 5. Preparation and Analysis of MTCS 38
5.1 Calibration of MTCS 38
5.2 Data reduction and analysis 40

Chapter 6. Interpretation of Experimental Results 43
6.1 Operation of the laboratory diffractometer 43
6.2 Experimental diffraction analysis of 3C-SiC 44

Chapter 7. Summary and Future Work 50
7.1 Summary 50
7.2 Future work 52

References 55

Appendices 58
Appendix A. DSO-1M X-ray diffractometer description 59
Appendix B. Radicon Device Programming Workbench 60
B.1 Speed bar 60
B.2 Installable Device Drivers 61
B.3 Radicon hardware server window 61
B.3.1 Controller window 62
B.3.2 High voltage unit window 63
B.3.3 Motor window 63
B.3.4 Power transmission of the step motor 65
B.3.5 Speed of rotation of the step motor 66
B.3.6 Operation points of the step motor 67
B.4 Angle encoder window 68
B.4.1 Position-sensitive detector window 70

المنارة للاستشارات
www.manaraa.com

B.4.2 Settings of the position-sensitive detector 71
B.5 Relays window 73
Appendix C. DSO-1M operation manual 75
C.1 Mechanical initialization 75
C.2 Instrument alignment 77
C.3 Detector calibration 80
C.4 Crystal lattice parameter measurement 82
Appendix D. Temperature Measurement Analysis 85
D.1 Real temperature estimation 85
D.2 Statistical measurement error 88
D.3 Measurement error estimation 91
D.4 Comparison of MTCS with other measurement techniques 93

المنارة للاستشارات
www.manaraa.com

List of Tables

Table 1. MTCS characteristics 9

Table 2. Macroscopic and X-ray densities of 3C-SiC irradiated at 100˚C [16] 26

Table 3. Final experimental results 49

Table 4. Brief characteristics of temperature measurements methods in hard to access places 51

Table B1. Motor's gear ratios 65

Table B2. Recommended frequency values for motors 67

Table B3. Encoder's gear ratios 69

Table C1. Pre-alignment conditions 77

Table D1. Temperature measurements and errors for MTCS at stationary regimes [30] 86

Table D2. Calculated values of linear regression and mean squared deviation of empirical data for MTCS [30] 87

Table D3. Parameters of α and β of the function $\sigma(T_M)$ for MTCS [30] 90

المنارة للاستشارات
www.manaraa.com

List of Figures

Figure 1.	a) MTCS size comparison; b) SEM micrograph of MTCS [8]	9
Figure 2.	Atomic model of 3C-SiC crystal	10
Figure 3.	Dependence of crystal lattice expansion of SiC on the neutron flux for different temperatures [5]	11
Figure 4.	Block-scheme of MTCS application [8]	12
Figure 5.	Single 3C-SiC crystal installation methods [10]	14
Figure 6.	Schematics of multi-crystal MTCS positioning in a rocket nozzle [10]	14
Figure 7.	Rocket engine combustion chamber turbo pump cross-section [10]	15
Figure 8.	Temperature gradient map of the “Buran” spacecraft [9]	15
Figure 9.	Stored energy per unit mass as a function of a crystal lattice expansion for irradiated 3C-SiC [16]	21
Figure 10.	Dependence of volume change, passed through a disturbance stage *k*-times, on time [5]	22
Figure 11.	Isochronous annealing of 3C-SiC irradiated at 100 ˚C [5]	29
Figure 12.	Crystal rotation axes	31
Figure 13.	Diffraction of X-rays by a crystal	32
Figure 14.	Schematic position of the 420 reflection plane in 3C-SiC	33
Figure 15.	Crystal rotation scheme	34
Figure 16.	Diffraction by a crystal rotated through the Bragg’s angle [25]	35

المنارة للاستشارات

www.manaraa.com

Figure 17. X-ray scattering in a fixed direction during crystal rotation 36

Figure 18. Calibration plot for 3C-SiC crystal lattice expansion as a function of annealing time and temperature [8] 39

Figure 19. Curves of isochronal annealing [8] 40

Figure 20. Temperature determination plot for MTCS at the non-stationary regime [8] 41

Figure 21. Photo of the lab diffractometer DSO-1M 43

Figure 22. Search of the beginning of a peak; 0.1˚ step 45

Figure 23. Maximum peak search; 0.05˚ step 46

Figure 24. Azimuth scan at ω_s=50.75˚; 1˚ step 47

Figure 25. Azimuth scan at ω_S =50.75˚; 0.5˚ step 48

Figure 26. Omega (ω_S) scan at the maximum intensity; 0.005˚ step 48

Figure 27. Isochronous annealing of diamond and 3C-SiC irradiated at the temperature of 196 ˚C and stored at 0 ˚C [5] 53

Figure A1. DSO-1M diffractometer 59

Figure B1. RDPW Speed bar 60

Figure B2. Radicon hardware server window 61

Figure B3. Controller window 62

Figure B4. High voltage unit window 63

Figure B5. Motor window 64

Figure B6. Mechanic tab; motor window section capture 65

Figure B7. Frequencies tab; motor window section capture 66

Figure B8. Motor’s operation points; motor window section capture 67

المنارة للاستشارات

www.manaraa.com

Figure B9. Motor's operation points scheme 67

Figure B10. Angle encoder window 69

Figure B11. Position-sensitive detector window 70

Figure B12. Settings window of position-sensitive detector 72

Figure B13. Calibration tab; position-sensitive detector window 73

Figure B14. Relays window 74

Figure C1. Initial data input window 76

Figure C2. Main form tab and the Relays sub tab 78

Figure C3. Photo of the measuring unit of the diffractometer DSO-1M 78

Figure C4. Calibration curve; position-sensitive detector window 81

Figure C5. Measurement input data 83

Figure D1. Estimation pattern of σ (SD) as a function of a measured temperature [30] 89

Figure D2. Standard deviation (σ) as a function of time 94

المنارة للاستشارات

www.manaraa.com

List of Nomenclature

a	crystal lattice parameter
z	zone volume
$\bar{\Sigma}$	microscopic section of average neutrons scattering
Ψ	neutron flux density
t	irradiation time
k	number of passes through a disturbance zone
E	energy
V	volume
ΔV	volume change
V_k	volume of material passed through a disturbance stage (zone) *k*-times
$V_{k,max}$	maximum volume of material passed through a disturbance zone
V^*	total volume of material passed through a disturbance zone *k*-times
N	point defect concentration
$\bar{\nu}$	average number of displacements per one neutron collision
T_{irr}	irradiation temperature
ΔT_{irr}	activation degree of neutron irradiation
N_C	number of elementary unit cells
ΔN_C	number of additional unit cells
C	concentration of point defects
C_v	concentration of vacancies
C_i	concentration of interstitials
C_F	Frenkel pairs concentration
$(\Delta\rho/\rho)_m$	variation of macroscopic density
$(\Delta\rho/\rho)_x$	variation of X-ray density

المنارة للاستشارات
www.manaraa.com

a_i	interstitials contribution to a crystal expansion
a_v	vacancies contribution to a crystal expansion
a_F	Frenkel pairs contribution to a crystal expansion
r	interatomic distance
n	bond order
θ	Bragg's diffraction angle
ω	rotation angle about vertical axis
φ	azimuth rotation angle
ω_s	sample's rotation angle about its vertical axis
θ_d	detector's rotation angle about its vertical axis
λ	wavelength
d	lattice plane spacing
h,k,l	Miller's indices
$Fe\text{-}K\alpha$	iron X-ray source
n	Bragg's law integer
$FWHM$	Full Width Half Maximum
N_a	total plane's length
$\xi_{1'2'}$	X-ray path length difference
T	annealing temperature
T_{max}	maximum annealing temperature
I_{max}	maximum intensity (counts)
$I_{\max}^{rev}$	maximum intensity per sample's revolution
I_{BG}	background noise level
T_M	measured temperature
T_{real}	real temperature
$L^{(\pm)}$	estimated measured temperature limit
$L^{(+)}$	upper estimated measured temperature limit
$L^{(-)}$	lower estimated measured temperature limit
f_{exp}	experimental function of measured temperature
δ	temperature measurement error

المنارة للاستشارات
www.manaraa.com

q	measurement's order
$T_{M,q}$	measured temperature at q measurement
$T_{real,q}$	real temperature at q measurement
$\Delta_{c,q}$	systematic temperature measurement error
a, b	linear regression values
ΔR_1, ΔR_2	mean squared deviations of temperature measurements
σ	standard deviation (SD)
i	subsample number
N_i	subsample volume
α_i, β_i	estimated regression parameters for the i-series
T_M^{eff}	effective (measured) temperature
T^{ub}	unbiased real temperature estimation
P	real temperature values portion
$\Phi_0(x)$	normalized Laplace's function
T_i^{Δ}	transient condition temperature
T_{i+1}^{Δ}	the nearest temperature
$T_N^{\Delta} - T_1^{\Delta}$	measured temperature range

المنارة للاستشارات
www.manaraa.com

Irradiated Single Crystal 3C-SiC as a Maximum Temperature Sensor

Viacheslav G. Kuryachiy

ABSTRACT

A neutron flux on the order of $2 \cdot 10^{20}$ neutrons/cm^2 at 0.18 MeV induces formation of point defects (vacancies and interstitials) in single crystal 3C-SiC causing a volume lattice expansion (swelling) of over 3% that can be measured by X-Ray diffraction. The crystal lattice can be completely restored with an annealing temperature equal to or higher than the irradiation temperature. This phenomenon serves as a basis for temperature measurements and allows the determination of the maximum temperature, if the exposure time is known.

The single crystal 3C-SiC sensor is applicable to small, rotating and hard to access parts due to its size of 300-500 microns, wide temperature range of 100-1450 °C, "no-lead" installation, inert chemical properties and high accuracy of temperature measurements. These features make it possible to use the sensor in gas turbine blades, automotive engines, valves, pistons, space shuttle ceramic tiles, thermal protection system design, etc.

This work describes the mechanism of neutron irradiation of single crystal 3C-SiC, the formation of point defects and their concentration, the different temperature measurement techniques, and the application of Maximum Temperature Crystal Sensors (MTCS) for maximum temperature measurements in both stationary and non-stationary regimes.

www.manaraa.com

Chapter 1

Introduction

Building more efficient engines and better thermal protection design are two important challenges facing the automobile and the space industries. The engine efficiency increases with the operating temperatures rise, which is limited by materials properties. New high-temperature materials are being developed and include high-temperature alloys, composites, and ceramic materials. Since material strength decreases with temperature, it is essential to develop adequate cooling systems that are efficiently monitored by thermal sensors. As the maximum operating temperature is normally just under a hundred degrees below the maximum temperature allowed for a particular material, it is extremely important to gain knowledge of the temperatures reached by operating devices.

Today, with the appearance of more complex devices, the design requirements for temperature sensors become more demanding. It is challenging to measure temperatures of machine elements because of many factors. Among them are high operating temperatures, large temperature gradients and the complexity, geometry and decreasing size of engine elements. In addition, the thermal sensor should not interfere or disturb the integrity of engine elements or their thermal properties.

All experimental temperature measurements are based on some sort of property or matter state change. It is a pressure of a fluid, volume of a fluid, electric resistance of a material, electric force induced by two dissimilar materials in contact and others. There are over thirty different phenomena and material properties used for measuring temperature [1], with even a larger number of temperature measurement tools available today. There is a vast variety of applications that have the need for new methods, enhanced measurement range, better accuracy, further reduced sensor size, etc.

المنارة للاستشارات
www.manaraa.com

Technical progress is determined mostly by the development of energy supplies, both stationary and mobile. One of the major characteristics for these supplies is a coefficient of efficiency defined by the operation temperatures. Usually, these temperatures can be accurately determined experimentally. For this reason, accurate temperature measurement techniques become especially important during the engine design, testing and fine tuning.

1.2 Statement of work

The current work is aimed for the development of a procedure for adjustment and precision alignment of the DSO-1M X-ray diffractometer for the accurate 3C-SiC crystal lattice parameter measurements. Discussion of the measurement results is presented. The developed methodology is described and used for measuring the neutron irradiated 3C-SiC lattice parameter, which enables one to determine the maximum temperature of the single crystal 3C-SiC sensor.

The work reviews both the theoretical and practical aspects of utilizing the single crystal 3C-SiC as the Maximum Temperature Crystal Sensor (MTCS). The theoretical part discusses the neutron irradiation and X-ray diffraction analysis of 3C-SiC turning it to the MTCS sensor. The practical part presents the X-ray diffraction results of the MTCS sensor proving its capability of using as a maximum temperature sensor. The DSO-1M X-ray diffractometer adjustment and alignment procedures are given in the appendices.

Chapter 2 through Chapter 5 contain review of the current knowledge in the field of single crystal 3C-SiC neutron irradiation and its use for high temperature measurements. The neutron irradiation influence on the 3C-SiC crystal lattice is discussed, describing the mechanism of crystal volume expansion due to vacancies-interstitials formation.

Chapter 6 presents the X-ray diffraction analysis of the neutron irradiated single crystal 3C-SiC. Here, the procedure for measuring the Bragg's angle by the DSO-M1

www.manaraa.com

X-ray diffractometer is described. The Bragg's angle obtained from the X-ray diffraction analysis is used to calculate the crystal lattice parameter of the MTCS sensor.

Summary of the conducted work and future outlook of the MTCS technique and ways for its improving are outlined in Chaper 7.

1.3 Hard to access parts temperature measurement tools

Temperature measurement methods in hard to access parts are divided in two categories based on their readout mechanism: contact and non-contact. The use of either one depends on the actual application. Each category has its corresponding advantages and disadvantages.

The contact readout mechanism category includes devices that have an electrical connection between a temperature sensor fixed on a part and a stationary readout device. While these units are complex and expensive, they are able to conduct continuous measurements during stationary and transient regimes. There is also an opportunity for using automation with the contact units, for example, to disconnect a unit at dangerously high temperatures. Contact readout devices are thermocouples, resistance sensors, thin-film resistance sensors, single and twin-lead thin-film resistance sensors [2].

Thermocouples and resistance sensors have minimal measurement errors and have a wide application range. However, their use with relatively small parts has great disadvantages. When thermocouples are installed on such parts, real temperature readings can be significantly distorted due to disturbances in heat exchange conditions with the environment. Thermo-electric heterogeneity of thermocouples over their length at high temperature gradients also increases the measurement error. High temperature gradients limit the application of resistance sensors due to averaging the temperature over time [2, 3].

Micro thermocouples are produced by drawing the wire thermocouples, covered with the organic-silicon insulation and placed inside a stainless capillary tube. The final diameter of the thermocouple is about 0.33 mm. The sensor is very flexible, and can be

المنارة للاستشارات
www.manaraa.com

easy installed in the device. One of the installation techniques is placing the sensor inside specially prepared channels. Micro thermocouples are limited in application for small-size parts that are subject to loads due to their weakening by channel making [2].

Surface thin-film resistance sensors are deposited in the form of thin films on a substrate made of a non-conductive layer. A disadvantage of the sensors is that the film structure is sensitive to environment influence. Furthermore, there is a temperature averaging over the film's area making the temperature measurements not accurate [4].

Single and twin-lead high temperature thin-film resistance sensors are produced by deposition of insulation layers made of enamels, heat-resistant cement or metal oxides. A hot junction of the thin film resistance sensor is deposited directly on the measured surface. It provides a reliable contact between a film resistance sensor and a measured part. Thickness of the high temperature thin-film resistance sensors ranges from 0.01 to 0.1 mm. Due to these small changes; they do not distort the temperature of measured parts. A disadvantage of the sensors is their sealed area, which becomes a source of additional voltage transmitted from the sensor; this occurs due to a difference in thermo-electric properties between the film and a wire made of the same material. This additional voltage depends on the temperature in the junction point. Therefore, it requires additional circuits or measuring temperature at this point. Some of the high temperature thin film resistance sensors are also not stable enough and are subject to the environment influence [5].

Non-contact readout devices include fusible metal thermometers, thermal paints, thermal plugs, Maximum Temperature Crystal Sensors (MTCS). The non-contact measurement methods allow the maximum temperature to be determined after the experiment is done; when the sensors are to be extracted from the measuring part and then analyzed later. These methods are not applicable for automation or temperature control and are not convenient for transient behavior studies. At the same time, they are indispensable for certain conditions where leading-out wires is very complex or not applicable.

Fusible metal sensors consist of a steel close-ended tube with metal or alloy insertions of different melting temperatures, spaced inside the tube. The insertions are

المنارة للاستشارات
www.manaraa.com

placed in order of increasing melting temperature. After a part is tested, the sensor is extracted, and then it is opened or X-rayed in order to determine the condition of the insertions. The maximum temperature of the tested part is defined by the melting temperature of two neighboring insertions – one fused and one unfused. It is obvious that the maximum temperature can be determined as close as an interval between the melting temperatures of the two neighboring insertions. This is the main disadvantage of the sensor. Furthermore, the size of the sensor is relatively large; thus, it is not applicable for temperature measurements of relatively small parts. In addition, there are some cases where none of the insertions are fused or, conversely, all of them are fused. If this happens, the observer can only conclude that the measured temperature was higher or lower a certain temperature dictated by the melting temperature if the spacers.

The thermal paint temperature measuring technique is based on changing the paint color depending on the temperature [6]. The main advantage of thermal paints is that they do not cripple a tested part. Among the disadvantages of the thermal paints are the aliasing of readings, the reading's sensitivity to the heating rate and exposure time at maximum temperature, unreliable results in hostile environments. Furthermore, thermal paints may fall due to vibrations of the tested parts.

The thermal plug temperature measuring technique is based on the ability of certain austenitic steels to age depending on the temperature and exposure time [1, 7]. The aging consists on the appearance of additional phases and corresponding changes in material hardness. The temperature range is usually from 150 ˚C up to 800 ˚C. The temperature is defined by the size of the imprint on the sensor's surface left by the diamond pyramid tip during the hardness test. The temperature measurement error of this method is ± 20 ˚C; and the plug size is 2.5x2.5x2.5 mm^3. A disadvantage of the method is the inability to produce a large number of thermal plugs with similar properties.

Surface temperature measurements can also be conducted using a method where the radioactive ^{85}Kr tracer is introduced into the part by ion bombardment or by heating the part in ^{85}Kr vapor under high pressure. After that, the part saturated with the ^{85}Kr tracer is tested under operating conditions, undergoing the annealing at gradually increasing temperatures. During this process, the annealing temperature and the amount

المنارة للاستشارات
www.manaraa.com

of escaping ^{85}Kr gas are controlled. When the temperature becomes higher than the temperature at which the part was tested, the leaving amount of radioactive ^{85}Kr gas increases rapidly. This temperature is considered as the testing temperature. The advantage of this method is that there is no chemical or physical crippling of the tested part. The disadvantage is the highly complex process of saturation the part with the ^{85}Kr gas [5].

Another surface temperature measurement technique, used in hard to access parts is the pyrometer method. The main disadvantage of the method is that the pyrometers can only test surface temperature. In addition, the absolute temperature measurement error can be quite large.

One of the advanced temperature measuring techniques is the Maximum Temperature Crystal Sensor (MTCS). Both diamond and 3C-SiC can be used in MTCS, which work in a similar manner. MTCS are primarily used for measuring the maximum temperature in stationary conditions. The non-stationary conditions, when the temperature changes with time, can be also measured using MTCS if the temperature variation with time is known. The maximum temperature that can be measured with diamond is about 900 C˚, while 3C-SiC MTCS are capable of measuring temperatures up to 1400 ˚C.

المنارة للاستشارات
www.manaraa.com

Chapter 2

The Maximum Temperature Crystal Sensor

2.1 Material selection for MTCS

The Maximum Temperature Crystal Sensor (MTCS) was developed by the Kurchatov Institute of Atomic Energy in Moscow, Russia. The MTCS measuring technique is based on the phenomenon of high temperatures to restore a crystal lattice changed by neutron irradiation. The materials used for MTCS must satisfy the following requirements:

1. significant crystal lattice expansion due to neutron irradiation;
2. small determination error of the crystal lattice expansion;
3. wide temperature range for crystal lattice restoring;
4. insignificant material's radioactivity caused by neutron irradiation;
5. ability to produce a large amount of sensors with similar properties.

There are many materials which experience a crystal lattice change due to neutron irradiation, namely: 3C-SiC, diamond, graphite, beryllium oxide, alumina oxide, boron nitride, boron carbide and some others. The most suitable materials for using in MTCS are 3C-SiC and diamond. Both materials have similar properties, and work in a similar manner. However, they have different temperature ranges; 3C-SiC is capable of measuring the temperatures in the range of 100 – 1400 ˚C, while the range for diamond is 100 – 900 ˚C. Moreover, synthetically produced diamonds and natural SiC and all their modifications cannot be used for MTCS due to their impurities which get activated by neutron irradiation causing radioactivity [5]. All these features make 3C-SiC more attractive to the current work and future research. At a temperature of about 100 ˚C, a

www.manaraa.com

neutron flux on the order of $2*10^{20}$ neutron/cm^2 (E>0.18MeV) causes a lattice volume expansion in 3C-SiC of up to 2.5-3%. The volume expansion error is about 0.01 – 0.02%. A crystal lattice starts shrinking after expansion at the temperatures of 100–1400 ˚C (annealing). This temperature range determines the operational range of the 3C-SiC sensor.

The impurities, which contribute to radioactivity of the 3C-SiC after neutron irradiation are ^{125}Sb, ^{113}Sn and ^{60}Co. These elements belong to the "B" group of radioactivity, and according to the safety rules, their overall allowable radioactivity for the workplace is 10 μCi or $3.7*10^5$ radioactive decays per second [5]. The amount of the impurities is so small, that it is allowed to work with 60,000 MTCS without special precautions. The stability of the 3C-SiC crystal lattice along with the uniformity of its properties changes during neutron irradiation and annealing makes it possible to produce a large amount of sensors with similar properties.

The single crystal 3C-SiC temperature sensor has been proven to be one of the best measuring devices for applications including large temperature gradients, high complexity and geometry of tested elements. Understanding how the sensor works requires the examination of several topics, which are directly related to a sensor usage, namely irradiation, annealing and X-ray diffraction.

2.2 Technical characteristics of MTCS

Single crystal silicon carbide has been extensively studied and used in various applications due to its unique physical, chemical and mechanical properties. In electronics, 3C-SiC is a possible replacement for silicon for high temperature, high power and high frequency applications. It performs well in a radioactive environment, as it hardly gets activated due to neutron bombardment. A good knowledge of 3C-SiC behavior during and after irradiation is a prerequisite for all the applications listed above. In fact, during neutron irradiation, lattice atoms are displaced, resulting in the formation of structural defects such as interstitials and vacancies.

المنارة للاستشارات
www.manaraa.com

3C-SiC is now a favored sensor material due to its high melting temperature of 2830 ˚C, inert properties, and extreme hardness. MTCS characteristics are listed in Table 1. A size comparison photo of MTCS and its scanning electro microscope micrograph are shown in Figure 1.

Table 1. MTCS characteristics

Measured temperature range	100 – 1400 ˚C
Maximum use temperature	1450 ˚C
Maximum heating/cooling rate	< 200 ˚C/sec
Exposure time range	1˚C – 1450 ˚C
Measuring accuracy (standard deviation)	± 15 ˚C
Sensor size	0.3 – 0.5 mm
Density	3.21 g/cm^3
Chemical stability in acids and bases	Stable
Lead wire / connectors	No required

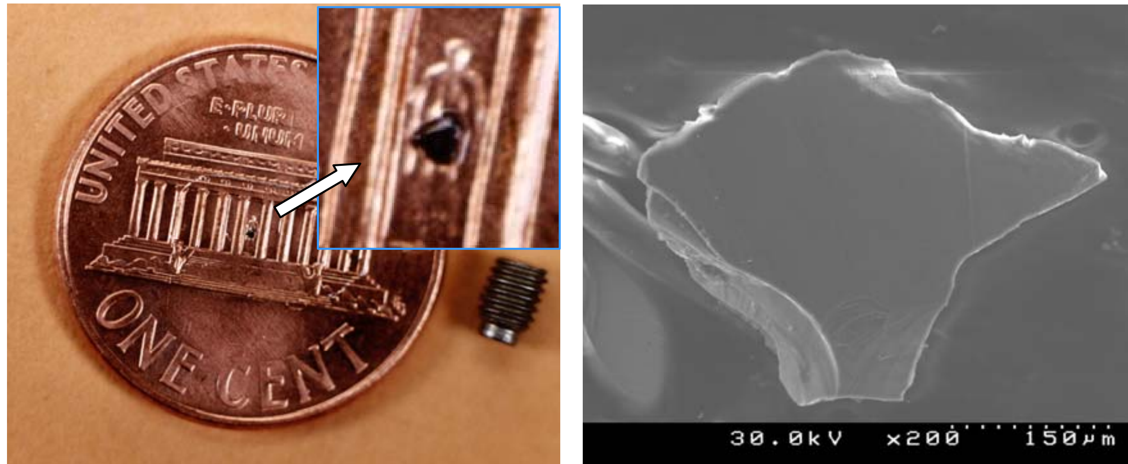

a) b)

Figure 1. a) MTCS size comparison; b) SEM micrograph of MTCS [8]

المنارة للاستشارات
www.manaraa.com

2.3 Manufacturing of MTCS

Both powder and grains of 3C-SiC up to 0.4 mm in diameter can be used for MTCS. The structure of the 3C-SiC may be considered as two face-centered cubic lattices stacked one into another. One of these face-centered cubic lattices is composed of carbon atoms, another of silicon atoms. Four silicon atoms surround each carbon atom. Silicon atoms, in turn, are surrounded by four carbon atoms (Figure 2).

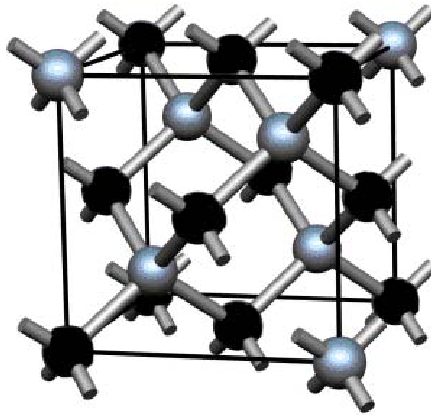

Figure 2. Atomic model of 3C-SiC crystal

The lattice parameter *a*, for a strain-free 3C-SiC is equal to 4.3608 Å. Bonds between carbon and silicon atoms in 3C-SiC are covalent, each atom shares one of its electron with the neighboring atoms.

Before a sensor becomes MTCS, it needs to be irradiated by neutrons in a nuclear reactor. The value of a neutron-flux, necessary for irradiation, is defined by the condition for large enough swelling of a crystal lattice, and on the other hand, it is defined by the condition of a limitation in the mean-square displacement of atoms. The growth originated by this displacement causes a lattice parameter alteration.

As seen in Figure 3, for a small neutron-flux F at 0.18 MeV, in the beginning of irradiation the crystal lattice parameter of 3C-SiC increases linearly. After defects concentration reaches a certain point, the linear increase of the lattice parameter continues with a lower slope [5].

المنارة للاستشارات
www.manaraa.com

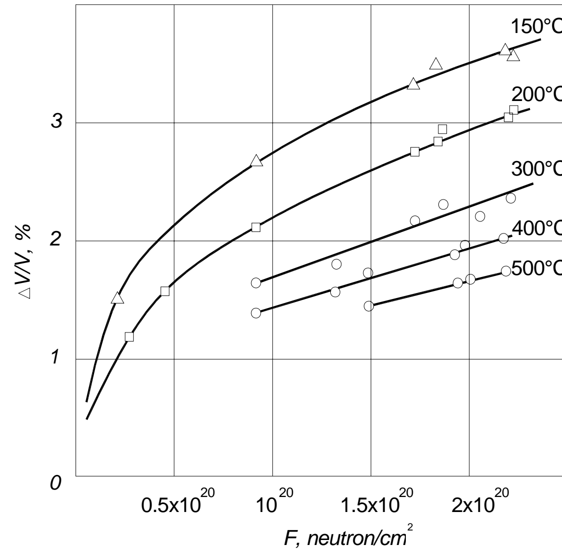

Figure 3. Dependence of crystal lattice expansion of SiC
on the neutron flux for different temperatures [5]

The mean-square displacement of atoms in a crystal lattice during irradiation depends on the neutron-flux value, and increases slightly in the beginning. Then, at the flux of $3 \cdot 10^{20}$ neutrons/cm^2 a drastic rise is observed. The optimal neutron-flux value, obtained from experiments, is about $(2 - 3)*10^{20}$ neutrons/cm^2 at 0.18 MeV. At these conditions, a crystal lattice swelling of 3C-SiC is large enough. The required time for irradiation can be calculated quite precisely due to the known neutron-flux density in the nuclear reactor.

For neutron irradiation, 3C-SiC is placed inside cassettes. The length and diameter of the cassettes should satisfy a condition of constant neutron-flux in terms of the cassette height and perimeter. It is necessary to provide such conditions during irradiation, where a difference in the lattice swelling throughout the whole volume of the cassette does not exceed 0.02%. In order to provide such a difference in the lattice swelling, the flux difference throughout the cassette's volume should not exceed $3*10^{18}$ neutrons/cm^2 or 2% from the overall irradiation dose. Because of this, irradiation always takes place in the middle of the nuclear reactor where the neutron-flux is more uniform [5].

المنارة للاستشارات
www.manaraa.com

Another important factor of MTCS manufacturing is the temperature of neutron irradiation. It is known that any material placed in a reactor becomes a source of heat due to γ-ray absorption. Therefore, this heat needs to be removed by cooling with water flowing through the cassette's center [5].

After a cassette with 3C-SiC is irradiated, it needs to be stored in a special repository. Storage is necessary to allow for the decay of short life isotopes accumulated in 3C-SiC inside a cassette during irradiation. The storing time is about 1 month. Then, the cassettes are opened inside a special box and the irradiated powder or crystals, extracted from the cassettes, undergo the following stages: washing in acids and distilled water, drying and calibration.

The amount of 3C-SiC irradiated in one cassette is usually about 5-10 g. This amount is enough to produce 50-100 thousand of MTCSs.

The application of MTCS can be described in the following stages, shown in Figure 4. First, the crystal has to be grown. Then it undergoes neutron irradiation followed by calibration. After the sensor is ready for temperature measurements, it can be installed in the tested part using different techniques. When the test is over, the sensor has to be extracted and examined separately. All these stages will be covered in the next several chapters.

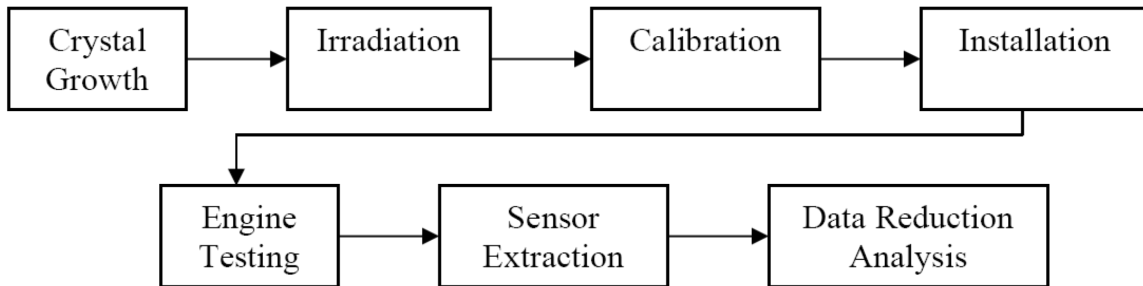

Figure 4. Block-scheme of MTCS application [8]

المنارة للاستشارات
www.manaraa.com

2.4 MTCS design and installation techniques

There are several designs of MTCS with different dimensions and different materials being used for temperature measurements. The design of MTCS is dictated by the dimensions of the tested part, the temperature to be measured, and other experimental requirements.

A capsule-type MTCS is a steel capsule with the ends welded and 3C-SiC crystals inside. Prior to welding one of the ends, a steel tab needs to be plugged between the sensor and this end to avoid annealing the sensor during welding. The capsule is usually made of a stainless steel; however, other materials may be used. The capsule is usually 5 mm long with 1 mm in diameter and may contain a mix of irradiated and unirradiated 3C-SiC powder. The unirradiated powder is used to decrease the measurement error.

The manufactured MTCSs are placed in plastic boxes labeled with the number of the irradiated powder's set they belong to. Each set has its own calibration diagram for temperature determination.

For temperature measurements of small-size parts, 3C-SiC powder can be directly placed inside a hole in the part. In this case, the volume of the temperature sensor can be decreased by a factor of 10 in comparison with the capsule-type MTCS. This method consists of drilling a small 1-2 mm deep and 0.5 mm diameter hole in the tested part. Then the hole is cleaned, degreased and filled with powder of irradiated 3C-SiC. It needs to be mentioned that unirradiated powder is to be added to the exposed 3C-SiC after the testing prior to the X-ray diffraction measurement. Then the hole is closed with a plug or pressure-contact-welded foil. Thus, it protects the powder from being blown away. Finally, the part is mounted into the machine and tested under the desired conditions [5].

Sometimes it is preferable to drill a hole at an angle. This method is recommended for temperature measurements of turbine blades and turbine disks [5]. In this case, the centrifugal forces press the powder to the bottom of the hole protecting it from being blown away. The length and diameter of the hole may be varied, but should have a volume equal to about 0.5 mm^3 necessary for placing about 1 mg of the 3C-SiC.

www.manaraa.com

Another way of using MTCS on a tested part is by installing 3C-SiC into machine parts using thermo-cement; and if necessary, the crystal is covered with nichrome foil (Figure 5). After the sensor is imbedded in a machine part, it is exposed to the test environment.

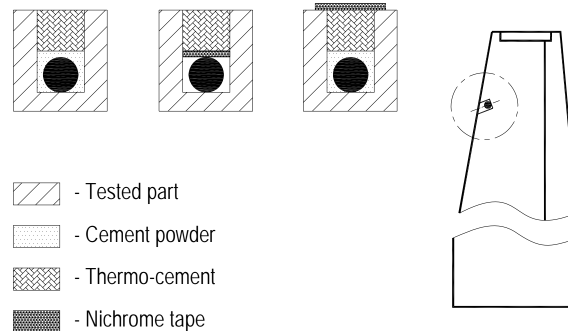

Figure 5. Single 3C-SiC crystal installation methods [10]

Besides single crystal MTCS there are also a multi-crystal MTCS. This type of sensor is designed for temperature gradient measurements. The sensor is manufactured as a 5 mm long steel capillary, with several 3C-SiC crystals inside spaced with steel spacers. One of the ends of such a capillary is marked in order to determine where the top or the bottom are and installed in the tested part.

Such multi-crystal MTCSs are widely used for temperature measurements in turbines, in rocket nozzles and spacecraft's shell. The positioning scheme for multi-crystal MTCS on the example of the rocket nozzle is shown in Figure 6.

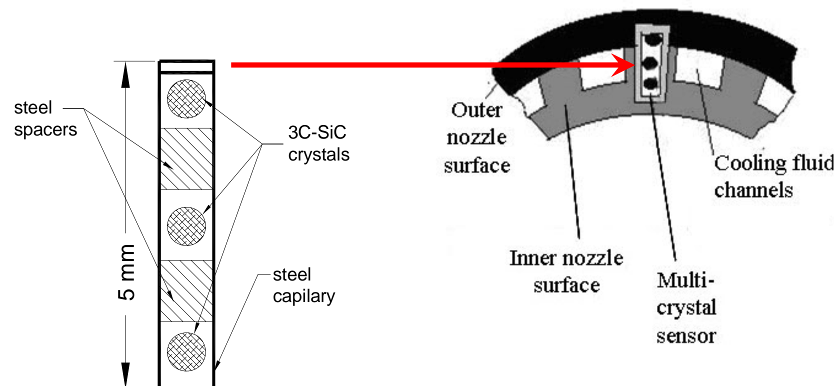

Figure 6. Schematics of multi-crystal MTCS positioning in a rocket nozzle [10]

المنارة للاستشارات
www.manaraa.com

The positioning scheme of MTCS on the example of the rocket engine combustion chamber turbo pump is shown in Figure 7. The numbers show the corresponding measured temperatures in ˚C.

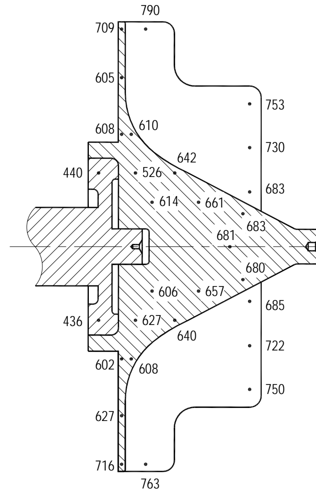

Figure 7. Rocket engine combustion chamber turbo pump cross-section [10]

Based on these temperature measurements obtained with the multi-crystal MTCS, the temperature gradient map can be obtained. Figure 8 shows the temperature gradient map of the "Buran" spacecraft's shell.

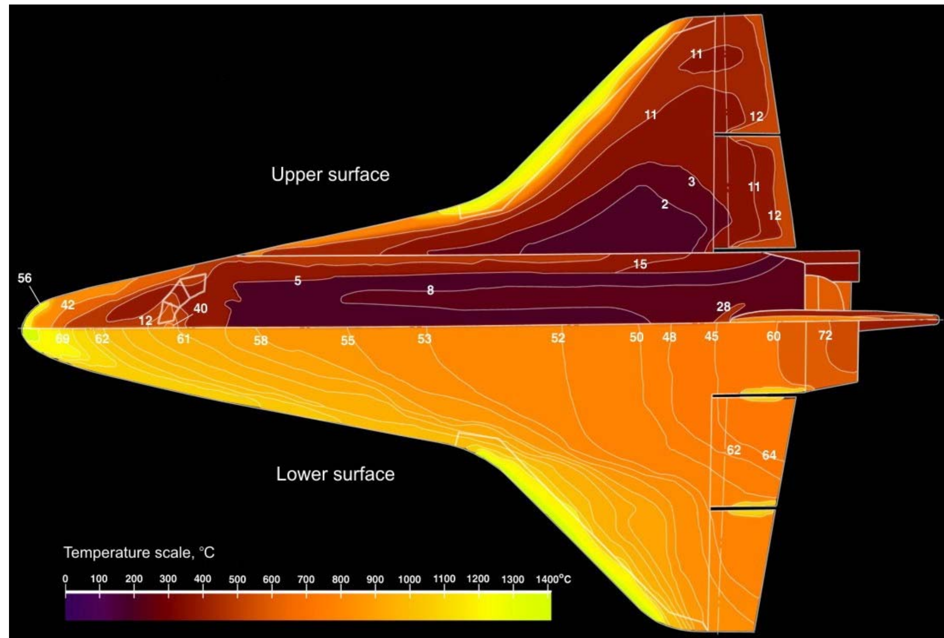

Figure 8. Temperature gradient map of the "Buran" spacecraft [9]

المنارة للاستشارات
www.manaraa.com

The temperature gradient map shows the temperatures that the spacecraft experiences while entering the atmosphere. There are two aircraft's surfaces shown on the gradient temperature map, the upper and the lower. The map shows that the highest temperature zones are on the leading edges of the wings and the nose of the aircraft entering the top layer of atmosphere at about a 40˚ angle from horizontal with its wings level. Such temperature gradient map is necessary for designing the aircraft's temperature protection system.

المنارة للاستشارات

www.manaraa.com

Chapter 3

Neutron Irradiation of Silicon Carbide

3.1 Features of neutron irradiation of materials

Neutron irradiation of materials has a great importance and practical significance in industry. Irradiation makes it possible to alter the properties of most materials in various ways by means of changing their microstructure. In the case of solid materials, these changes correspond to crystal lattice transformations.

Material irradiation with high-energy particles leads to imperfection – vacancies and interstitials, so called point defects or Frenkel pairs [5]. Defect appearance, hence structural alteration in most cases degrades the material's properties. On the other hand, this disadvantage may be used in a practical way. For example, here is a possibility of using a stored energy: defect appearance in a crystalline lattice of a solid body leads to excess energy. During annealing this energy is released. Therefore, graphite irradiated by high energy neutrons possesses stored energy, that when quickly released can warm up graphite by hundreds of degrees. It is a non-desirable property if a material is supposed to work in a nuclear reactor. On the other hand, the excess energy can be used in chemical reactions which require an additional heat source.

3.2 Principle of neutron irradiation

The principle of SiC sensor operation is based on the dependence of annihilated radiation defects on the exposure temperature and time. Therefore, it is important to look

المنارة للاستشارات
www.manaraa.com

at the irradiation mechanism, the type of defects created by neutron irradiation, their transformation and annealing.

In regards to the value of energy and irradiation type, materials experience the following effects: ionization, atom displacement in a crystalline lattice leading to Frenkel pairs formation (vacancy – interstitial), atom's substitution, displacement peaks (zones with high defects concentration), and nuclear transformation. These and some other effects lead to changes in material's physical and mechanical properties such as electrical conductivity, hardness, density, etc.

Heating of the irradiated material leads to the disappearance of some of the defects (Frenkel pairs); it also leads to the transformation of the defects. Among them are double-vacancies, complexes, extra planes and others. During this heating process, the properties of the material are partially restored. This process is called annealing.

Irradiation by electrons, protons, ions, γ – rays, etc. causes ionization and atom displacements. Atom displacements due to γ – irradiation are less possible, and present a secondary process in which electrons are knocked out by neutrons [5].

Neutrons do not have a charge, and consequently react directly with the atomic nuclei of the irradiated material. During collision, neutrons transport their energy to the nuclei and turn them into high-energy ions, causing ionization and new atom displacements.

During neutron irradiation the number of secondary, tertiary, quaternary, etc. knocked out atoms greatly exceeds the number of primary atoms. To estimate all these displacements, it is necessary to analyze the cascade process started by the primary atom. It is assumed that there is some displacement energy threshold, required to move atoms from their lattice cells. It may be defined as the minimal kinetic energy that has to be transferred to a lattice atom in order to create a stable Frenkel pair. This quantity is rather difficult to measure, since defects have to be identified during experiments, associated with well-defined irradiation energy [11]. So, if an atom in a crystalline lattice receives energy higher than the energy threshold, it gets displaced from its lattice site. If the gained energy is less than the energy threshold, no displacement takes place. In addition to the displacement energy threshold there is also, the so-called ionization energy

المنارة للاستشارات
www.manaraa.com

threshold. If a primary atom is knocked out, and has less energy than the ionization energy threshold, its energy is spent on elastic events (collisions). Therefore, there is a cascade of displacements and a region with high concentration of point defects at the end of the travel path of the neutron. This region is called a zone, or peak of displacement. The size of such a zone is 20-100 Å. During energy release, a substance in a zone is completely melted and some of the atoms leave this zone. Right after that the energy is released to a surrounded area. At the same time most of the created point defects recombine; however, the zone continues to be a high point defect density zone. Later on, a concentration of defects in the zone decreases due to thermal annealing. The annealing rate is controlled by temperature.

As neutron irradiation continues, the displaced atoms will continue to displace. This happens at the moment when the displacement zones overlap. Such a process leads to a dependence of defect concentration of the irradiation dose which is characterized by a saturation of defects.

However, a transformation of the point defects into more complex forms as well as existing in irradiated material and other effects make the results more complicated. A defect concentration cannot be simply quantified; therefore, a correlation between changes of material properties and defects' concentration has to be taken into consideration.

3.3 Atom displacement energy of irradiated 3C-SiC

Neutron irradiation alters electrical conductivity, hardness, density, and other physical and mechanical properties. One of the most important effects on 3C-SiC caused by neutron irradiation is the change of the crystal volume. When a vacancy is formed and the surrounded atoms are not relaxed, the knocked out atoms move from their original lattice sites and hence increase the crystal volume (density decrease). Conversely, with the formation of interstitials, the density of the material increases.

المنارة للاستشارات
www.manaraa.com

The amount of energy required to displace silicon and carbon atoms from their lattice sites to interstitial positions in SiC have been determined using molecular dynamic simulations and first principles calculations [12]. The values of displacement energies averaged over all directions in SiC have been determined to be 20 eV for carbon and 35 eV for silicon, and it is recommended that these values be used universally for calculating displacements per atom in irradiated SiC [13]. There are four minimum recoil damage energies required to create displacements in SiC, depending on the projectile/target combinations: 41 eV (C/Si), 35 eV (Si/Si), 24 eV (Si/C) and 20 eV (C/C). The minimum recoil damage energies for the C/Si and Si/C projectile/target combinations can be easily derived from the self-ion combinations. For example, a carbon atom must have kinetic energy of at least 41 eV to provide the 35 eV to a silicon atom that is necessary to displace it [14].

Perlado et al. [15] have also performed molecular dynamics simulations of neutron damage in 3C-SiC. They described a case of damage accumulation by "ductile" silicon sublattice and "fragile" carbon sublattice to express an outstanding capability of recombination of silicon recoils, as many more defects were produced on the carbon sublattice than on the silicon sublattice. These simulations treated the defects configurations after the cascade damage occurred.

3.4 Volume change of 3C-SiC due to neutron irradiation

As previously mentioned, point defects in a crystalline lattice cause a lattice parameter alteration and internal energy increase. Alterations of the lattice parameter and internal energy are proportional to the density of point defects. Figure 9 shows a dependence of the stored energy per unit mass on the lattice expansion for irradiated 3C-SiC [16]. It indicates that the lattice expansion (up to 3-4%) is proportional to the accumulated energy.

المنارة للاستشارات
www.manaraa.com

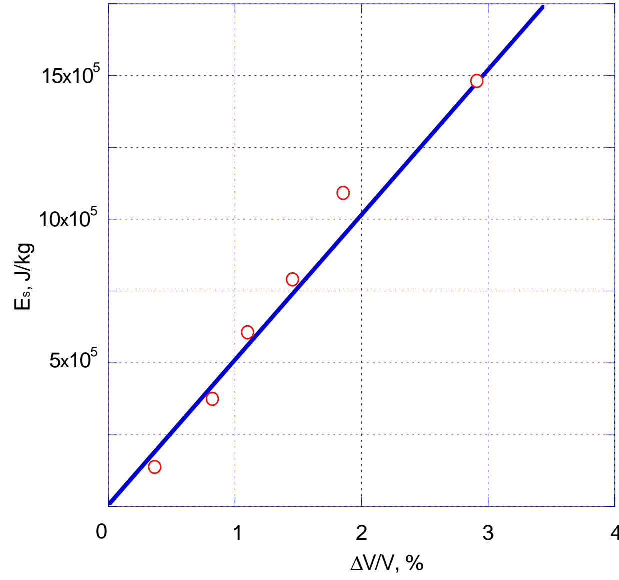

Figure 9. Stored energy per unit mass as a function of a crystal lattice expansion for irradiated 3C-SiC [16]

One of the most important factors influencing the degree of neutron irradiation is the temperature of irradiation. As the temperature rises, the activation of thermal defects increases. Because their concentration is decreasing, mechanical and physical properties change caused by irradiation becomes smaller. This effect is described in Figure 3, where it is shown that for the same energy flux, the higher the irradiation temperature, the smaller point defect density is [5].

Crystal lattice expansion of 3C-SiC is determined by both thermal and neutron irradiation annealing. As the irradiation exposure time increases, more material passes through the disturbance stage – peaks or displacement zones. During irradiation, some material regions pass through the disturbance stage twice, or more. These regions of a crystal as well as once disturbed regions have almost the same defect density.

The volume of material that passes through a disturbance stage (zone) *k*-times can be written as [5]:

$$V_k = \frac{\left(z\bar{\Sigma}\psi t\right)^k exp\left(-z\bar{\Sigma}\psi t\right)^k}{k}, \qquad (1)$$

المنارة للاستشارات
www.manaraa.com

where z - is the zone volume; $\overline{\Sigma}$ – is a microscopic section of average neutrons scattering; ψ – is the neutron flux density; t – irradiation time [5, 16].

The maximum amount of volume that passes through a disturbance zone 1, 2, 3,… k-times can be expressed as:

$$V_{k\,max} = k^{k-1} exp\left(-k\right). \tag{2}$$

The graphs, showing a dependence of V_k on radiation time for different number of passes k, are plotted in Figure 10 [1]. V^* - is a total volume of material passed through a disturbance zone k-times and is equal to V_k at all k-values. The curve V^* is shown as a dash line (Figure 10).

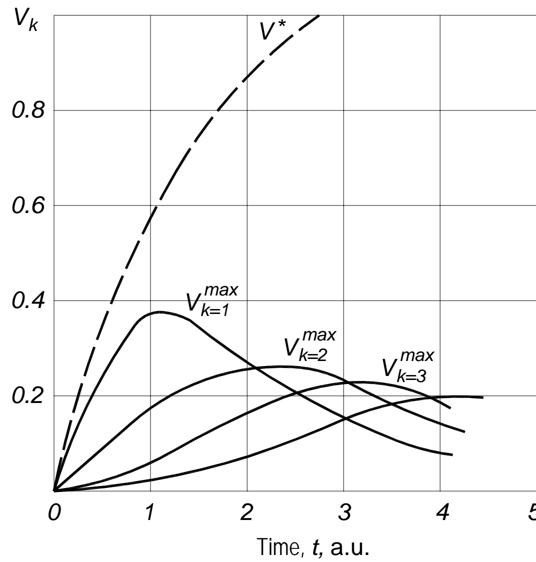

Figure 10. Dependence of volume change, passed through a disturbance stage k-times, on time [5]

The analytical expression of the curve is the following [5]:

$$V^* = \sum_{k=1}^{k=\infty} V_k = 1 - exp\left(-z\overline{\Sigma}\psi t\right). \tag{3}$$

المنارة للاستشارات
www.manaraa.com

If there was no thermal annealing, expression (3) would describe an expansion process of 3C-SiC due to neutron irradiation (experimental curves shown in Figure 3). However, the defect density in irradiated material is proportional to a number of zones and depends on their "age". The "older" the zone, the smaller the defect density is in this zone. This effect happens due to the thermal annealing of defects.

A concentration of the point defects can be also decreased by the influence of "bombarding" particles and secondary shifted atoms, whose energy is less than displacement energy but high enough for atoms to be activated [17]. Defect activation due to neutron irradiation occurs mostly by γ-irradiation. Such additional annealing of defects is equivalent to thermal annealing at a higher temperature. The differential equation, describing the point defects appearance in materials due to neutron irradiation, and also depending on the neutron flux density, irradiation temperature and γ – irradiation density, is written as [5]:

$$\frac{dN}{dt} = \psi \overline{\Sigma} \overline{\nu} \, [1 - \rho(T_{irr}, \Delta T_{irr})] - z \psi \overline{\Sigma} N \,, \qquad (4)$$

where N – is a point defect concentration at present time; $\overline{\nu}$ – is an average number of displacements per one neutron collision; $1 - \rho(T_{irr}, \Delta T_{irr})$ – is the probability of the displaced atom staying at its displaced position at the irradiation temperature T_{irr} and its corresponding degree of activation of neutron irradiation, ΔT_{irr}. ΔT_{irr} is determined by the ratio of the primary collision number to the overall collision number where atoms receive the energy smaller than the displacement energy threshold.

The probability $1 - \rho(T_{irr}, \Delta T_{irr})$ is determined experimentally by the slope of the curves in the beginning of irradiation (Figure 3). The first part of equation (4) describes defect accumulation; the second part describes the decrease of accumulation of defects due to irradiation annealing. The general solution of equation (4) is:

$$N(t) = [1 - \rho(T_{irr}, \Delta T_{irr})] \, \frac{\overline{\nu}}{z} \, [1 - exp\left(-z \overline{\Sigma} \psi \, t\right)] \,. \qquad (5)$$

المنارة للاستشارات
www.manaraa.com

In the beginning of 3C-SiC crystal expansion, the point defects concentration at neutron irradiation corresponds to equation (5). As the irradiation time becomes longer, deviation takes place – a monotonic increase is observed. This is described by the fact that at high concentration of point defects, the probability for complex defects to appear becomes higher, which, in turn, has a different effect on the lattice expansion [18, 19].

As the lattice expands beyond 14%, it is impossible to measure the lattice parameter of the irradiated 3C-SiC, but the macro-density keeps decreasing to 45% of the lattice expansion. At this point, 3C-SiC becomes amorphous.

The possibility of the presence of both point defects and more complex defects in the crystalline lattice makes the relationship between defects concentration and changed properties more complicated. However, if the lattice volume increase does not exceed 3-4%, contributions from the complex defects may be neglected, especially because the complex defects have a weak influence on the average crystal lattice parameter.

3.5 Point defects in 3C-SiC

The concentration of the point defects, interstitials and vacancies can be calculated by knowing the volume V of the specimen (3C-SiC crystal) and the crystal lattice parameter, a [20, 21]. The number of elementary unit cells in the ideal crystal with the cubic structure is:

$$N_C = V/a^3. \tag{6}$$

The formation of vacancies and interstitials in the crystal causes a change in volume. A number of additional cells created by the defects and their further relaxation can be calculated using the following expression:

$$\Delta N_C = \left(\partial N_C / \partial V\right)\Delta V + \left(\partial N_C / \partial a\right)\Delta a\,. \tag{7}$$

للاستشارات المنارة
www.manaraa.com

Substituting equation (6) into (7) gives:

$$N_C = \left(\frac{1}{a^3}\right)\Delta V - \left(\frac{3V}{a^4}\right)\Delta a \,. \qquad (8)$$

Dividing both parts of equation (8) by the cell number gives a relationship between the defects concentration and the crystal lattice parameter alteration [5]:

$$\frac{\Delta N_C}{N_C} = \frac{\Delta V}{V} - 3\frac{\Delta a}{a} \,, \qquad (9)$$

where $(\Delta V/V)$ represents a fractional variation of macroscopic density $(\Delta\rho/\rho)_m$ with the opposite sign; $(3\Delta a/a)$ is a fractional variation of X-ray density or the theoretical density taken with the opposite sign. The following equation is valid if there is only one type of defects in the crystal:

$$C = \left(\frac{\Delta\rho}{\rho}\right)_X - \left(\frac{\Delta\rho}{\rho}\right)_M \,, \qquad (10)$$

where C is a concentration of point defects; $(\Delta\rho/\rho)_m$ and $(\Delta\rho/\rho)_x$ are the variation of macroscopic and X-ray densities, respectively.

The variation of macroscopic and X-ray densities can be either negative or positive. If a part in the right side of equation (10) is positive, it means that a number of cells $\Delta N/N$ increases. In this case, C is a concentration of vacancies C_v. A negative number gives a concentration of interstitials, $C = C_i$ (a number of cells decreases).

The equilibrium of macroscopic and X-ray densities means that a number of cells is constant; hence, the concentration of vacancies is equal to the concentration of interstitials ($C_v = C_i$) [5].

Thus, to determinate the type and concentration of point defects, the macroscopic and X-ray densities have to be measured. The most accurate data obtained on single crystals, is shown in Table 2 [22, 16].

المنارة للاستشارات
www.manaraa.com

Table 2. Macroscopic and X-ray densities of 3C-SiC irradiated at 100˚C [16]

Density, %		F, 10^{20} neutrons/cm^2	Type		Density, %		F, 10^{20} neutrons/cm^2	Type
Macroscopic	X-ray				macroscopic	X-ray		
1.1	1.34	0.25	–		3.3	3.50	3.4	α
–	1.72	1.78	α		3.6	3.49	3.4	β
2.5	2.25	5	–		4.2	3.39	5.8	β
2.6	2.90	5.5	–		3.7	3.41	5.8	α
3.1	3.27	2.5	α		7.4	7.0	9.9	α
3.7	3.16	2.5	β		7.1	7.3	9.9	β
–	3.15	3.01	α		7.2	6.3	13.2	α
–	3.37	3.38	β		7.7	7.3	13.2	β

During annealing, the crystalline structure gradually shrinks to its original volume. However, annealing of highly irradiated 3C-SiC can lead to further expansion of volume. At this point, annealing works as if 3C-SiC was irradiated further [18, 23].

While annealing at normal (atmospheric) pressure of highly irradiated 3C-SiC decreases the crystalline structure volume, high pressure present during annealing leads to greater volume reduction. It is described by a presence of long-range order in the position and stacking sequence of atoms in the lattice of almost amorphous 3C-SiC.

3.6 Defect concentration in 3C-SiC

As already discussed, crystal lattice expansion occurs due to the formation of Frenkel pairs. In this chapter, the reasons for an increase of volume of crystal lattice will be discussed. An estimation of the contribution to a crystal expansion from both interstitials a_i, and vacancies a_v is presented. A relationship between Frenkel pairs concentration and crystal lattice expansion is established by [5]:

المنارة للاستشارات
www.manaraa.com

$$\frac{\Delta V}{V} = (a_i + a_v)\, C = a_F C\,. \tag{11}$$

Estimated non-dimensional values of a_i and a_v have been already presented in Konobeevsky's et al. work [21], where he explains the lattice expansion of carbon materials. When the vacancy is created, the neighboring atoms "draw" into the centers of trianguls, formed by the nearest atoms. Based on this idea, the estimated value of the Frenkel pairs contribution to the lattice expansion is $a_F = 0.6$ [21]. As it will be shown later, this approximation is very close to the real contribution.

Estimation of a_i and a_v values is based on the relationship between the interatomic distance *r* (in our case for 3C-SiC) and the bond order *n*, which shows the number of bonds between a pair of atoms. A function $r=f(n)$ must give a real interatomic distance if the bond order is known.

The number of point defects created at moderate neutron irradiation doses does not usually exceed several percent, and the original bonds are remained in a crystal. However, the bonds located nearby the defects are changed. To characterize these new bonds, the bond order must be assumed: an interstitial and a vacancy are electrically neutral; the interstitial atom's electrons and the electrons that are separated from the neighboring atoms to a vacancy are used to create new bonds within the first coordination surroundings.

In order to explain a swelling effect of 3C-SiC, it is required to examine the vacancy-interstitial contribution to the crystal lattice expansion.

When the interstitial atom is located in the center of a free octahedral site in the 3C-SiC lattice, a bond order created by this interstitial atom and its nearest surrounding atoms is $n = 0.5$ because its four free electrons are used to create four bonds. At $n = 0.5$ a distance between the central (interstitial) and corner atoms in the octahedral site will be $r = 1.99$ Å. When a volume of the octahedral site in the 3C-SiC lattice corresponds to the atomic volume, then it increases from 5.67 Å^3 to 12.23 Å^3 and leads to the value of $a_i = 1.16$ [5].

المنارة للاستشارات
www.manaraa.com

A vacancy position is determined by the position of a regular atom. When a vacancy is created, each of the four surrounding atoms loses one electron. These electrons are used to create bonds with the nearest three neighbors. The new bond order in these groups of atoms is n = 1.17 instead of n = 1.0. Consequently, the interatomic distance decreases (volume of the contact decreases from 5.67 $Å^3$ to 4.98 $Å^3$). A vacancy is surrounded by eight smaller octahedral sites, four of which are shrinking and the other four remain unchanged. So, $a_v = -0.49$ [5].

V.M. Koshkin et al. [24] speculate that the atoms next to a vacancy are more likely to be shifted towards the vacancy due to rapidly growing repulsive forces if the atoms move towards the neighboring atoms. That is why the overall crystal volume decreases mostly due to the volume of vacancies, and due to surface tension effects, the absolute volume of vacancies should always be less than the volume of the interstitials. A simple correlation gives a contribution of vacancies in the 3C-SiC compression, $a_v = -0.61$.

The total contribution of the Frenkel pairs to lattice expansion is $a_F = a_i + a_v = 0.67$. Interstitials expand the crystal lattice while vacancies cause shrinking. Since neutron irradiation on 3C-SiC causes the formation of Frenkel pairs, lattice expansion occurs. The coefficient a_F = 0.67 makes it possible to determine the concentration of the Frenkel pairs based on the experimental lattice expansion value:

$$C_F = \left(\frac{\Delta V}{V}\right) / a_F = 1.47 \frac{\Delta V}{V} . \qquad (12)$$

3.7 Annealing temperature of irradiated 3C-SiC

During neutron irradiation of materials, defects are induced mostly due to high-speed neutrons, and by high-speed electrons created by γ-rays. Electrons turn defects into a different state, changing their activation energy. Therefore, depending on the intensity

المنارة للاستشارات
www.manaraa.com

of γ-irradiation accompanying neutron-irradiation, the defects annealing rate changes. This rate is determined by the activation energy spectrum.

An increase of the irradiation dose leads to a defect density rise, which in turn causes a decrease of the annealing rate. One reason for this is that a defect density rise causes a higher probability appearance of more stable complex defects with high activation energy.

Experiments prove that the crystal lattice parameter of 3C-SiC starts changing when the temperature of isochronous annealing reaches the temperature under which the crystal was irradiated [17]. Figure 11 shows that 3C-SiC starts shrinking at a temperature equal or higher than the irradiation temperature of 100 ˚C. In case of irradiation with a higher temperature, a break point of the isochronous annealing curve would also coincide with the irradiation temperature.

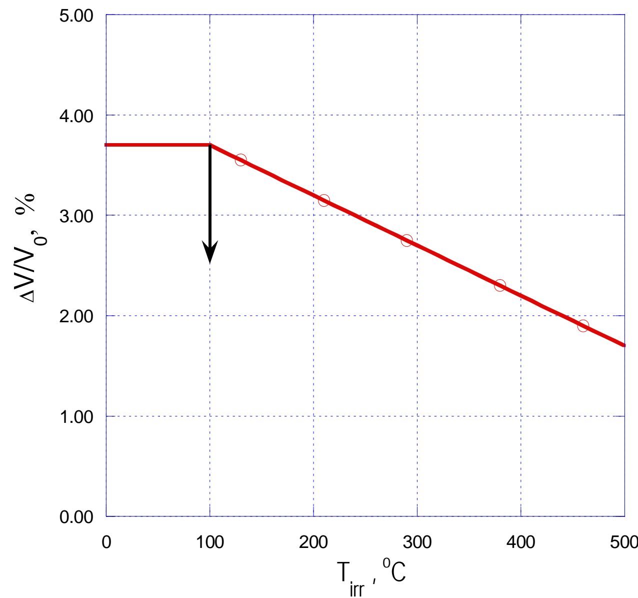

Figure 11. Isochronous annealing of 3C-SiC irradiated at 100 ˚C [5]

المنارة للاستشارات
www.manaraa.com

Chapter 4

Diffraction Analysis

4.1 Diffractometer method

Determination of the unknown spacing of crystal planes requires a diffraction analysis. The diffraction analysis can be performed with a diffractometer which uses X-rays of known wavelength.

Single crystal specimens such as 3C-SiC can be examined in a diffractometer by mounting the crystal on a goniometer which will allow independent rotation of the specimen and a detector about the diffractometer axis and another axis passing through the specimen.

In the diffractometer, a single crystal will produce a reflection only when its orientation is such that a certain set of reflecting planes is inclined to the incident beam at a 2θ angle. Assuming, that a reflection is produced, the inclination of the reflecting planes with respect to any chosen line or plane on the crystal surface is known from the crystal position. Two kinds of operations are required:

1. Rotation of the crystal about various axes until a position is found for which reflection occurs;
2. Location of the normal to the reflecting plane on a stereographic projection from the known angle of rotation.

The diffractometer method has many variations, depending on the particular type of goniometer used to hold and rotate the specimen. The diffractometer used in the current work is equipped with a sample holder, which provides the possible rotation axes

المنارة للاستشارات
www.manaraa.com

shown in Figure 12: one coincides with the diffractometer axis (ω), while the other (BB') is normal to the specimen surface (φ). I – is an incident beam; *D* – a diffracted beam; *C* – a specimen; *S* – slits.

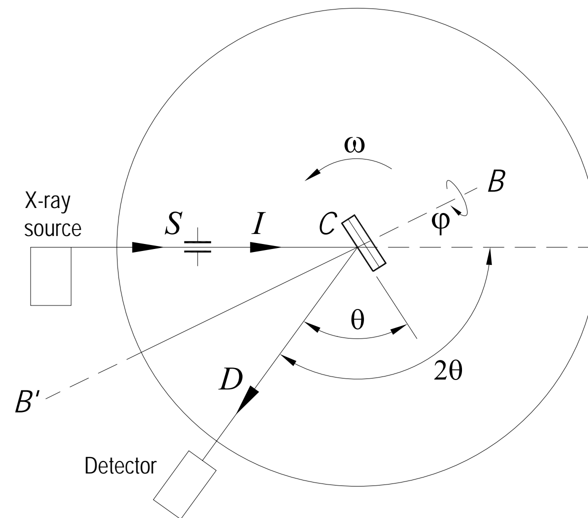

Figure 12. Crystal rotation axes

The diffractometer method is faster than many other methods such as the Laue, the Guinier-Tennevin [25, 26], the Lang and the Borrmann methods [31]. Furthermore, using narrow slits in order to reduce the divergence of the incident beam can yield results of greater accuracy. However, using extremely narrow slits will make it more difficult to locate the reflecting positions of the crystal, or to direct the incident beam upon the target as in the current work.

4.2 Application of Bragg's law

Experimentally, Bragg's law can be applied in two ways. By using X-rays of known wavelength λ and measuring θ, it is possible to determine the spacing d of various planes in a crystal. Alternatively, the radiation wavelength λ can be determined for a crystal with planes of known spacing d_{hkl} and measured θ (Figure 13). In the current

المنارة للاستشارات
www.manaraa.com

work, the first approach has been utilized in order to determine the lattice parameter of the 3C-SiC crystal, and hence, the volume expansion of the crystal. The target (anode) element used as the X-ray source is Fe-Kα with a wave length of 1.936 Å and was selected in order to give the best accuracy in comparison with other widely used X-ray sources such as Cu-Kα (λ=1.541 Å) or Cr-Kα (λ=2.291 Å) [31].

$$n\lambda = 2d_{hkl}\sin\theta\,, \tag{13}$$

where n – is an integer. For all cases of interest, it is allowed to take $n = 1$ and write the expression (13) as follows [26]:

$$\lambda = 2d_{hkl}\sin\theta\,. \tag{14}$$

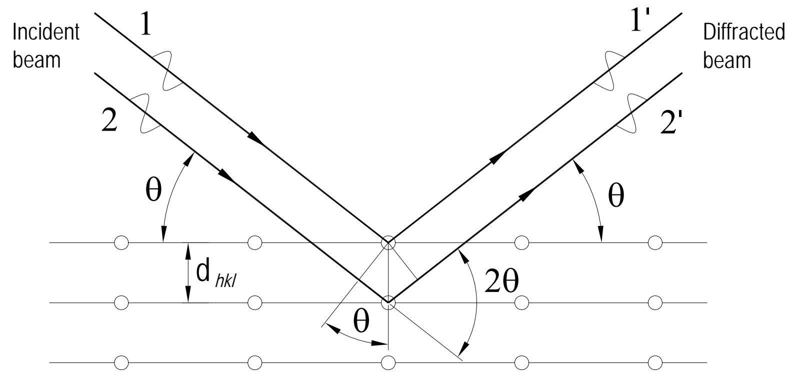

Figure 13. Diffraction of X-rays by a crystal

The measuring procedure consists of the following steps:

1. MTCS is mounted on the X-ray diffractometer in the path of the X-ray beam;
2. The crystal is illuminated with X-ray and the diffraction angle is recorded;
3. The *d*-spacing is calculated using Bragg's law.

The X-ray diffractometer used in the current work is described in the appendix A and is designed to measure 3C-SiC single crystals 420 reflections (Figure 14).

المنارة للاستشارات
www.manaraa.com

The value of d, the distance between adjacent planes in the set (hkl), can be found from the following equation for the cubic structure [26]:

$$\frac{1}{d_{hkl}{}^{2}} = \frac{(h^2 + k^2 + l^2)}{a^2}. \tag{15}$$

Combining Bragg's law and equation (15) yields:

$$\sin^2 \theta = \frac{\lambda^2}{4a^2}(h^2 + k^2 + l^2). \tag{16}$$

For a particular incident wavelength λ and a particular cubic crystal with a unit cell size a, this equation predicts all the possible Bragg angles at which diffraction can occur from the (hkl) planes. For 420 planes, the equation (16) becomes [26]:

$$\sin^2 \theta_{420} = \frac{5\lambda^2}{a^2}, \tag{17}$$

$$a = \frac{\lambda}{\sin \theta_{420}} \sqrt{5}. \tag{18}$$

A schematic position of the 420 reflection plane in 3C-SiC single crystal is shown in Figure 14.

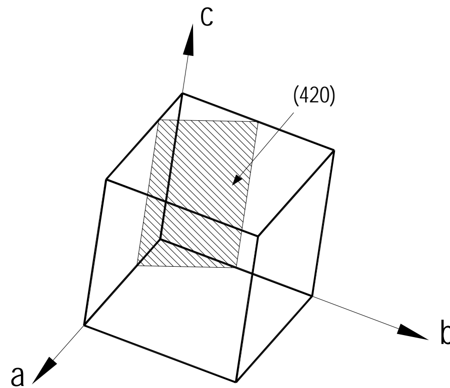

Figure 14. Schematic position of the 420 reflection plane in 3C-SiC

المنارة للاستشارات
www.manaraa.com

In order for the diffracted X-ray beam from the 420 plane to be registered by the detector, the crystal must be rotated to the position where diffraction occurs. The position of the 3C-SiC crystal where the diffraction occurs is schematically shown in Figure 15. The position of the crystal is described by the XYZ coordinate system. Both, the detector's and the crystal's rotations are controlled by the goniometer. The detector is located at the $2\theta_d$ angle, while the 3C-SiC crystal rotates at ω and φ angles till the diffraction is found. This rotation of the 3C-SiC crystal is sufficient to obtain the diffraction from the 420 reflection plane of the crystal by the detector positioned at the $2\theta_d$ angle. The incident X-ray beam (1′) hits the 3C-SiC crystal and diffracts (2′) from the 420 reflection plane at the 2θ angle. At this condition, the crystal's 420 reflection plane would be located at the θ angle with the YZ axis (Figure 15).

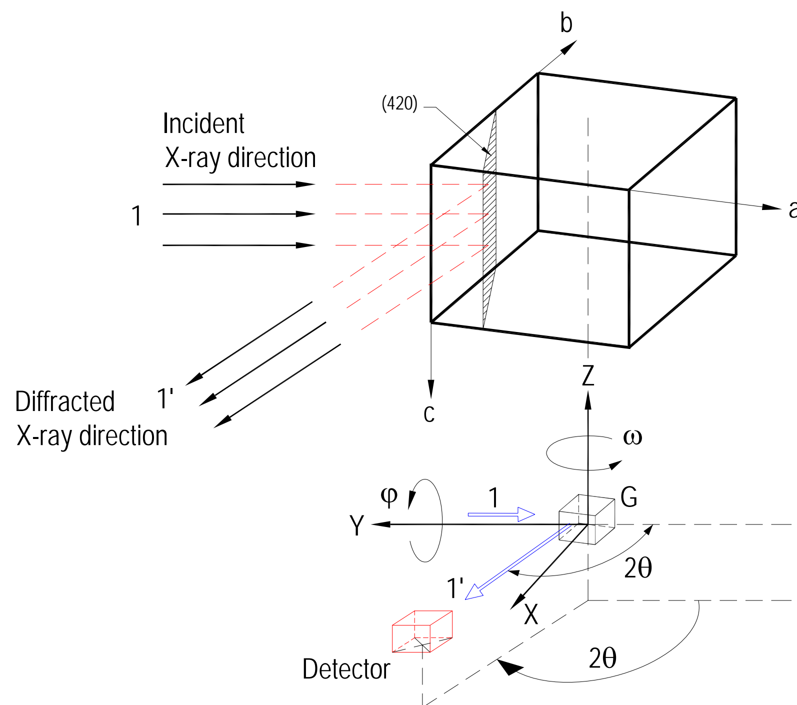

Figure 15. Crystal rotation scheme

www.manaraa.com

4.3 Lorenz factor

In order to understand how the peak or the maximum intensity is created, it is necessary to consider certain trigonometrical factors which influence the intensity of the reflected beam. Suppose there is a narrow X-ray beam on a crystal, and let the crystal be rotated at a uniform angular velocity about an axis through C and normal to the drawing, so that a particular set of reflecting planes, assumed for convenience to be parallel to the crystal surface, passes through the angle θ_B, at which Bragg's law is exactly satisfied (Figure 16a). The intensity of reflection is greatest at the exact Bragg's angle but still appreciable at angles deviating slightly from it, so that the curve of intensity vs. 2θ is of the form shown in Figure 16b. If all the diffracted beams are registered by the detector, one can calculate the total energy of the diffracted beam by integrating the curve. This energy is called the integrated intensity of the reflection (Figure 16b).

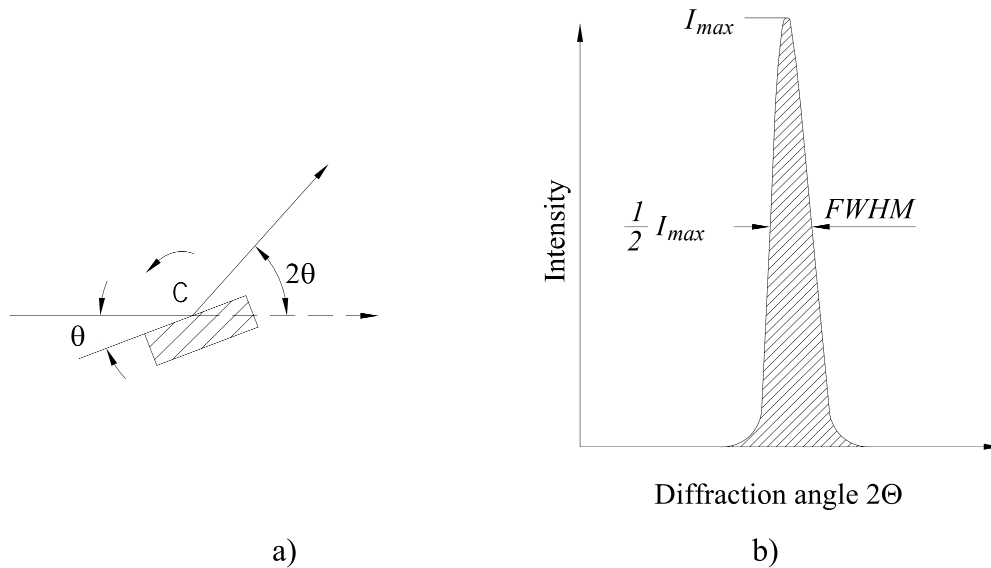

Figure 16. Diffraction by a crystal rotated through the Bragg's angle [25]

The integrated intensity of a reflection depends on the particular value of θ_B. It is possible to find this dependence by considering separately two aspects of the diffraction curve: the maximum intensity and the Full Width Half Maximum (FWHM).

المنارة للاستشارات
www.manaraa.com

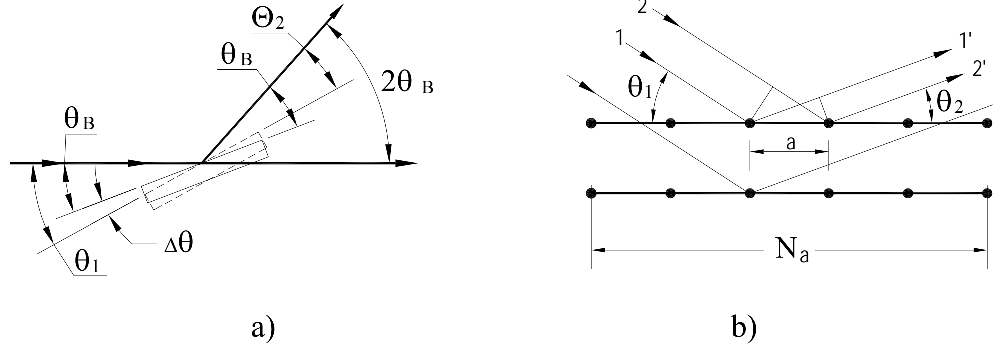

Figure 17. X-ray scattering in a fixed direction during crystal rotation

When the reflecting planes make an angle θ_B with the incident beam, Bragg's law is satisfied and the intensity of the diffracted beam is the maximum. But some energy is still diffracted when the angle of incidence differs slightly from θ_B. The value of I_{max} therefore depends on the angular range of crystal rotation over which the energy diffracted in the θ_B direction is appreciable. In Figure 17a, the dashed lines show the position of the crystal after rotation through a small angle $\Delta\theta$ from the Bragg position. The incident and the diffracted beams make unequal angles with the reflecting planes: the former making an angle $\theta_1 = \theta_B + \Delta\theta$ and the latter $\theta_2 = \theta_B - \Delta\theta$. This case is shown in Figure 17b, where it is allowed to consider only a single set of planes, since the rays scattered by all the planes are in phase with the corresponding rays scattered by the first plane. Let a be equal to the atom spacing in the plane and N_a the total length of the plane. The difference $\xi_{1'2'}$ in path length for rays 1' and 2' scattered by adjacent atoms is given by equation" (19) [25]:

$$\xi_{1'2'} = AD - CB = a\cos\theta_2 - a\cos\theta_1 = a[\cos(\theta_B - \Delta\theta) - \cos(\theta_B + \Delta\theta)]. \qquad (19)$$

By expanding the cosine terms and setting sin($\Delta\theta$) equal to $\Delta\theta$, for small $\Delta\theta$ ($\Delta\theta < 1^\circ$) . Then, $\xi_{1'2'}$ can be expressed as:

$$\xi_{1'2'} = 2a\Delta\theta\sin\theta_B. \qquad (20)$$

المنارة للاستشارات
www.manaraa.com

The path difference between the rays scattered by atoms at either end of the plane is simply N_D times this quantity. When the rays scattered by the two end atoms are one wavelength out of phase, the diffracted intensity will be zero. The condition for zero intensity is therefore [25]:

$$2N_D a \Delta\theta \sin\theta_B = \lambda , \tag{21}$$

or :

$$\Delta\theta = \frac{\lambda}{2N_D a \sin\theta_B} . \tag{22}$$

This equation gives the maximum angular range of crystal rotation over which appreciable energy will be diffracted in the $2\theta_B$ direction. Since I_{max} depends on this 2θ range, it would be proportional to $1/\sin(\theta_B)$. Other things being equal, I_{max} is therefore large at low scattering angles and small in the region of back reflected X-rays.

The breadth of the diffraction curve varies in the opposite way, being larger at large values of $2\theta_B$, where the FWHM was found to be proportional to the product I_{max}, which is in turn proportional to $(1/\sin\theta_B)(1/\cos\theta_B)$ or to $1/\sin2\theta_B$. Thus, as a crystal is rotated through the Bragg's angle, the integrated intensity of a reflection turns out to be greater for larger and small values of $2\theta_B$ than for intermediate values [25].

المنارة للاستشارات
www.manaraa.com

Chapter 5

Preparation and Analysis of MTCS

5.1 Calibration of MTCS

The calibration process consists of annealing irradiated crystals at known temperatures and different times. The basic requirements for calibration are the precise setting and maintaining of the annealing temperature, the exposure time measurement during annealing, and the crystal lattice volume change measurements. The crystal volume change is obtained from the crystal lattice parameter measuring using the diffractometer method described in the previous chapter.

A plot used for determination of the temperature, measured by MTCS is a series of isotherms plotted every 10 ˚C. The abscissa serves as an exposure time expressed by a logarithmic scale in minutes, and the ordinate serves as the lattice expansion expressed in percent.

To plot such a graph it is necessary to test about one hundred sensors from irradiated 3C-SiC set. First, they are exposed to annealing at constant time (isochronous nnealing) in the range of 100 – 1300 ˚C. The exposure time is 1, 10, 10^2, 10^3, and sometimes 10^4 minutes. After the annealing, 3C-SiC undergoes X-ray analysis and the results are used for plotting a graph (Figure 18).

The principles used for plotting the graph are the following: the annealing is to be done in increasing steps of 50 ˚C. After each annealing an X-ray analysis is taken and the crystal lattice parameter is measured. The results are then plotted where the abscissa shows the annealing temperature and the ordinate shows the percentage of the crystal

المنارة للاستشارات
www.manaraa.com

volume change. The points of each isochronous annealing are to be outlined with a smooth curve shown in Figure 18.

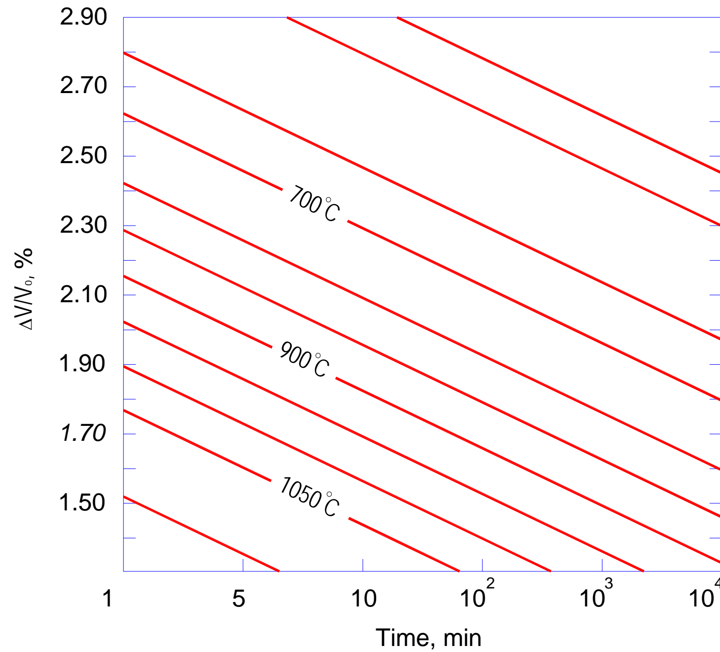

Figure 18. Calibration plot for 3C-SiC crystal lattice expansion as a function of annealing time and temperature [8]

It is obvious that for MTCS sensors the temperature measurement error depends on the accuracy of plotting the graph. The absolute error when measuring the annealing temperature should not exceed ±2 ˚C. A temperature perturbation at any point of exposure time cannot exceed ±1 ˚C; accuracy of the exposure time duration must be less than ±5%. The measurement error of the 2θ diffraction angle of MTCS must be less than ±2'.

The graphs of isochronous and isothermal annealing have to be drawn in scale without distortion of the temperature, the exposure time and the crystal lattice parameter alteration expressed in the crystal volume change.

المنارة للاستشارات
www.manaraa.com

5.2 Data reduction and analysis

As mentioned in earlier chapters, the principle of operation of the 3C-SiC sensor is based on the annealing of point defects created by neutron irradiation. The Frenkel pairs cause crystal lattice expansion. The distance between the Frenkel pairs is variable. Depending on this parameter, they have different annealing activation energy. Due to this phenomenon, defects in the irradiated 3C-SiC are annealed gradually with the temperature increase. At this, the crystal lattice shrinks.

There is a functional relationship between three parameters: lattice volume expansion, temperature and exposure time. If the exposure time is known, and the lattice volume expansion after annealing is known, the temperature can be determined. Vice versa, if the temperature and the expansion are known, the exposure time can be determined (Figure 19).

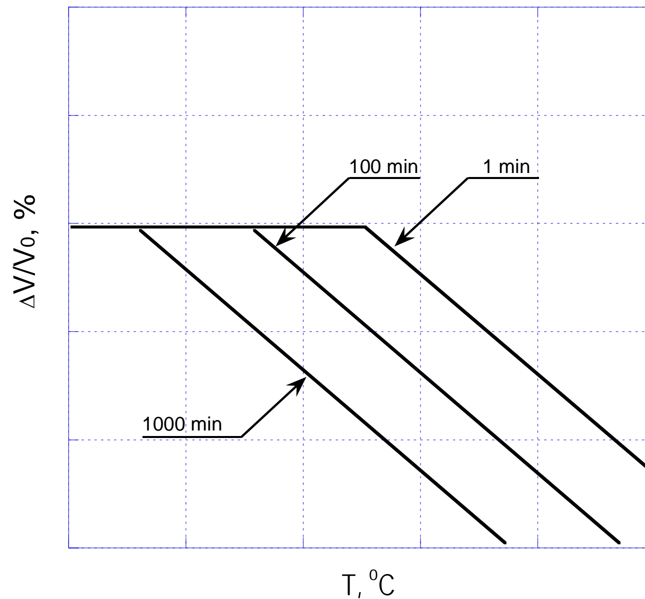

Figure 19. Curves of isochronal annealing [8]

Figure 20 shows the crystal volume expansion $\Delta V/V$ as a function of the exposure time at the maximal temperature T, expressed in logarithmic scale.

المنارة للاستشارات
www.manaraa.com

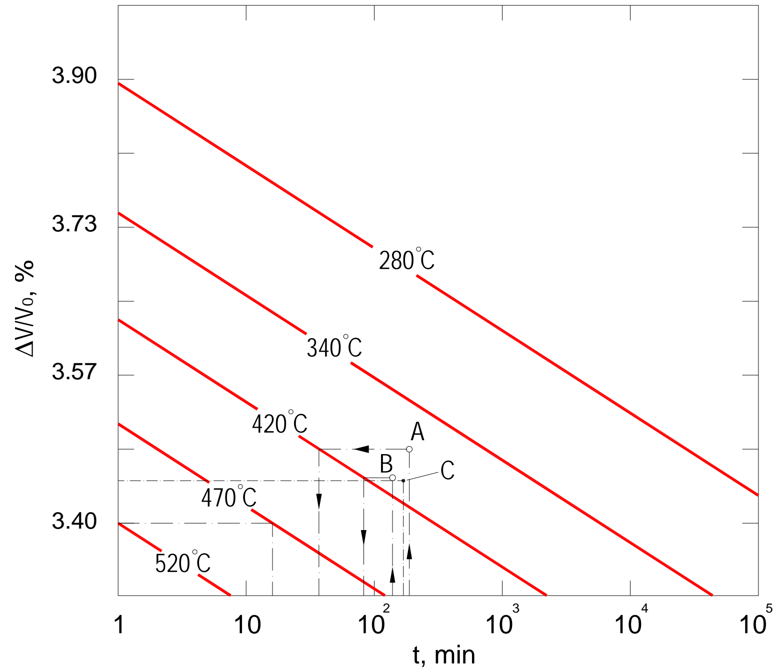

Figure 20. Temperature determination plot for MTCS
at the non-stationary regime [8]

The temperature, at which the sensor was exposed, is defined by the isotherm at the intersection of the exposure time t, and the crystal lattice expansion $\Delta V/V_0$.

Let us assume that the sensor is exposed to the maximum temperature for 30 minutes. A lattice expansion of 3.4% corresponds to the maximum temperature of 470 ˚C.

This way of finding the maximum temperature is applicable for a stationary heating regime. However, it is important that the sensor can also work at more complicated non-stationary regimes, where the temperature is changing during the test. In this case, MTCS is exposed to the maximum temperature during a certain period of the overall testing time. Therefore, it is necessary to take into consideration the effect of the annealing at lower temperatures, and introduce the appropriate corrections to determine the maximum temperature.

The same value of the crystal lattice expansion of 3C-SiC can be obtained by annealing at different temperatures and different exposure times.

المنارة للاستشارات
www.manaraa.com

Consider an example where a tested part was heated to T_{max} for 100 minutes, then to 95% of T_{max} for 150 minutes, and then to 90% of T_{max} for 300 minutes, resulting in the total lattice expansion of 3.49% which corresponds to 420 ˚C. First, the approximate upper bound of the maximum temperature achieved in 100 minutes for the lattice expansion of 3.49% needs to be determined. According to the plot, shown in Figure 20, a crystal lattice expansion of 3.49% corresponds to 420 ˚C. This temperature is assumed as the maximum temperature T_{max}=420 ˚C. Then all the relative temperatures are to be converted to the absolute temperatures: 100 minute exposure at 420 ˚C, followed by 150 minute exposure at T=0.95 T_{max}=399 ˚C, followed by 300 minute exposure at T=0.90*T_{max} = 378 ˚C. It should also be noted that the lattice expansion decrease caused by the exposure of 378 ˚C for 300 minutes is equivalent to 60 minute exposure at T_{max}=420 ˚C (point A in Figure 20). Similarly, annealing at the temperature of 399 ˚C for 150 minutes is equivalent to a 90 minute anneal at 420 ˚C (point B). Therefore, this particular non-stationary heating regime is equivalent to the maximal temperature anneal for 100 + 60 + 90 = 250 minutes. This would be an equivalent time of 250 minutes anneal at the maximum temperature T_{max} as the non-stationary annealing gives the same result in terms of the crystal lattice expansion change. Now, the maximum temperature of 370 ˚C is determined from the lattice parameter change, expressed in the crystal lattice expansion of 3.49 % and the equivalent time of 250 minutes (point C). The equivalent time is always less then the actual testing time, but greater than the time of exposure at the maximum temperature.

المنارة للاستشارات
www.manaraa.com

Chapter 6

Interpretation of Experimental Results

6.1 Operation of the laboratory diffractometer

An X-ray diffractometer DSO-1M used for measuring the diffraction angle and hence a lattice parameter value of 3C-SiC single crystals, is shown in Figure 21. The diffractometer and the operational software "Radicon Device Programming Workbench" (RDPW) were developed by Radicon Inc. in Saint-Petersburg, Russia. The diffractometer was designed to measure the lattice parameter of 3C-SiC single crystals by the diffraction from its 420 reflection plane. The procedure of finding the reflection plane was schematically shown in Chapter 4.

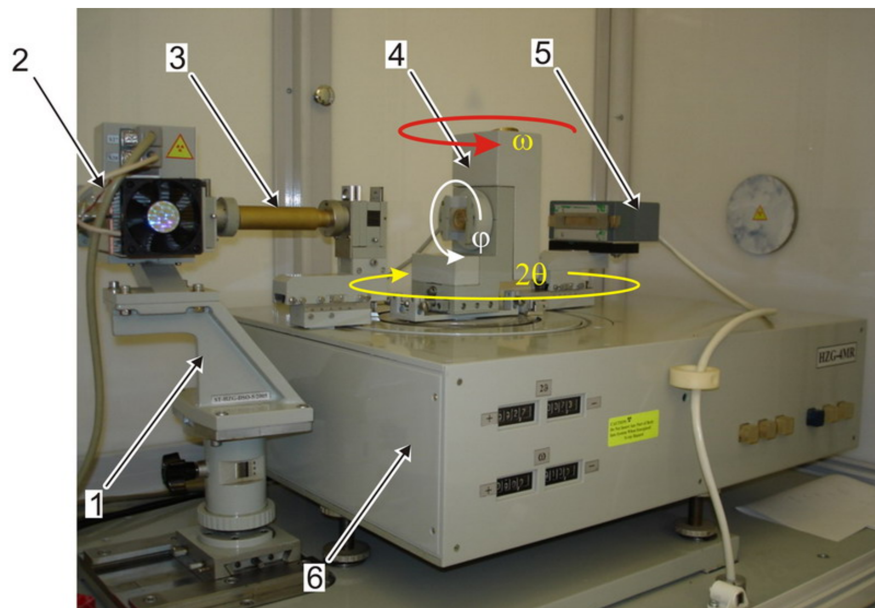

Figure 21. Photo of the lab diffractometer DSO-1M

المنارة للاستشارات
www.manaraa.com

The diffractometer DSO-1M consists of the following units: 1 – adjustable column; 2 – X-ray source unit; 3 – collimator tube; 4 – sample holder; 5 – detector; 6 – goniometer; 7 – X-ray generator (not shown); 8 – control block (not shown). A detailed description of the diffractometer' operation and the software is given in Appendix A and Appendix B, respectively.

The samples are inserted inside the specially designed cuvettes made of plastic or plexiglass with a hole drilled in the center. The holes are designed for different size crystals and have a range of 0.3-0.6 mm. A detailed procedure of the sample's installation is given in the Appendix C.4.

The sample holder is capable of rotation about its vertical axis at angle ω_s and is also capable of providing rotation of the sample at angle φ. The detector is rotated at the angle $2\theta_d$ equal to 162.5˚ while a sample holder is rotated at the angle ω_s=50˚. The Bragg angle (θ) of the original not irradiated 3C-SiC is about 83.1˚, and therefore 2θ =166.2˚. The detector's position at $2\theta_d$ =162.5˚ and its registration range of ±6.0˚ is sufficient to register the diffraction of the Bragg's angle at θ =83.1˚.

6.2 Experimental diffraction analysis of 3C-SiC

The measuring procedure consists of finding the diffracted beam maximum intensity at the fixed position of the detector $2\theta_d$ and the variable sample angle ω_s. Using Bragg's law, the crystal lattice parameter of 3C-SiC is calculated from the angle θ that corresponds to the found maximum intensity. The measurement is based on the 420 reflection from 3C-SiC crystal lattice and is carried out in a fully automated manner.

The measurement starts with a launching the software "Radicon Device Programming Workbench" (RDPW) and running the macro command "Measure". The program will ask to name a sample and specify the measuring mode. The measuring mode consists of either finding a diffraction angle of the X-ray beam from the sample or finding the intensity values for a range that can be manually specified. The initial angle scanning positions for the sample (ω_s) is equal to 50˚ with a 0.1˚ scanning step, while the

المنارة للاستشارات
www.manaraa.com

detector's center is fixed at the angle $2\theta_d$=162.5˚. The entire measurement procedure may be divided into several steps described below.

1. Positioning of the sample and the detector at the 50˚ and 162.5˚ angles, respectively.

2. Adjusting the high-voltage power supply of the X-ray tube to 25 kV, 2 mA.

3. A preliminary search of the intensity peak. The sample is rotating at the azimuth angle φ with the rate of 1/6 rev/sec; ω_s rotation of the sample with a step of 0.1˚ (Figure 21). Every step is followed by searching the maximum intensity per every revolution of the sample. The scanning stops when the maximum intensity I_{max} becomes higher than a background noise level I_{BG} by the value of the square root of its value (23):

$$I_{max}^{rev} > I_{BG} + \sqrt{I_{BG}} \,. \tag{23}$$

The inequality (23) is an empirical constrain which was obtained in order to register the actual maximum (peak) and disregard the false peaks.

The detector is fixed at the 162.5˚ position (θ_d); the specimen is at the 50˚ position (ω_s), the step is 0.1˚. The results are shown in Figure 22.

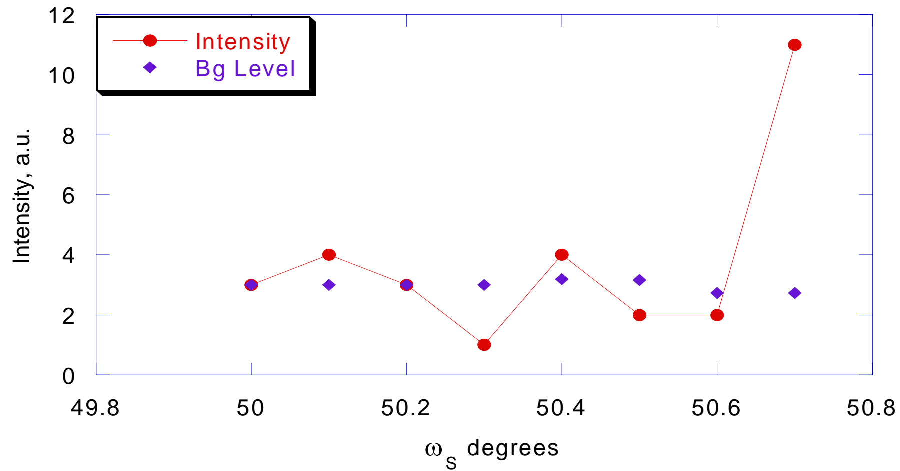

Figure 22. Search of the beginning of a peak; 0.1˚ step

المنارة للاستشارات
www.manaraa.com

The maximum found intensity is 11 photons/sec that corresponds to ω_s =50.70˚ (Figure 22).

4. Confirmation of the peak. Analogous to step 3 except for the azimuth φ rotation of the sample with the rate of 1/30 rev/sec and the ω_s rotation with a step of 0.05˚. If the background noise level rise is not found after three steps, the procedure returns to step 3. Otherwise, it proceeds to the next step.

5. Search for the peak end at φ rotation the sample at 1/30 rev/sec. Stepping of the ω_s rotation of the sample is 0.05˚. The maximum intensity value is registered for every step. Search for the ω_s, corresponding to the maximum intensity per revolution of the sample. The scanning process stops when the empirical constrain (24) is reached [5]:

$$I_{max}^{rev} < I_{\max} - 2\sqrt{I_{\max}}, \tag{24}$$

where I_{max}^{rev} - is the maximum intensity per revolution of the sample; $I_{\max}$ - is a maximum intensity over three 0.05˚ steps. A rough determination of the sample position for the angle φ happens when the peak is observed. The accuracy of the angle φ is ±15˚. The results of the maximum peak search are shown in Figure 23.

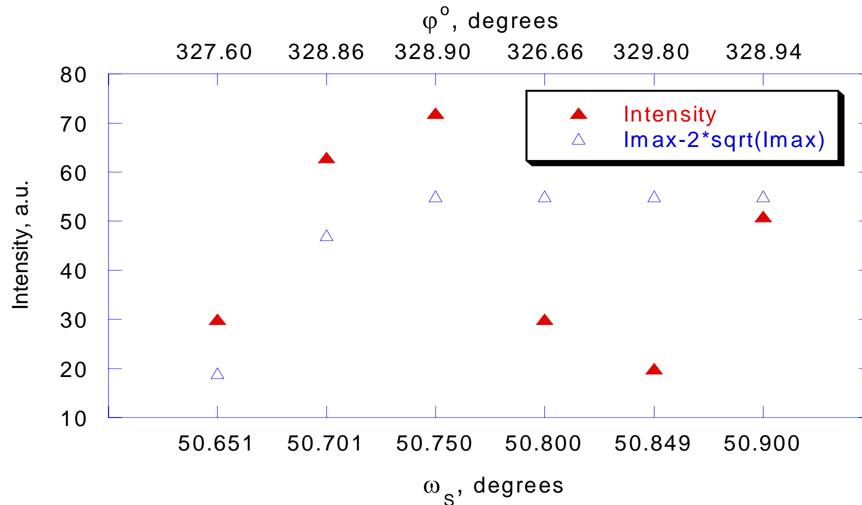

Figure 23. Maximum peak search; 0.05˚ step

المنارة للاستشارات
www.manaraa.com

The rough φ and ω_s positions for the sample at the maximum intensity are 328.90˚ and 50.750˚ respectively (Figure 23).

6. Positioning of the sample at the ω_s and the φ corresponding to the maximum value of intensity found in the previous steps: $\omega_s = 50.750$, $\varphi = 328.90$.

7. Azimuth (φ) scanning in 1˚ increments. Determination of the φ angle position of the sample at the maximum intensity and fixed ω_s (Figure 24).

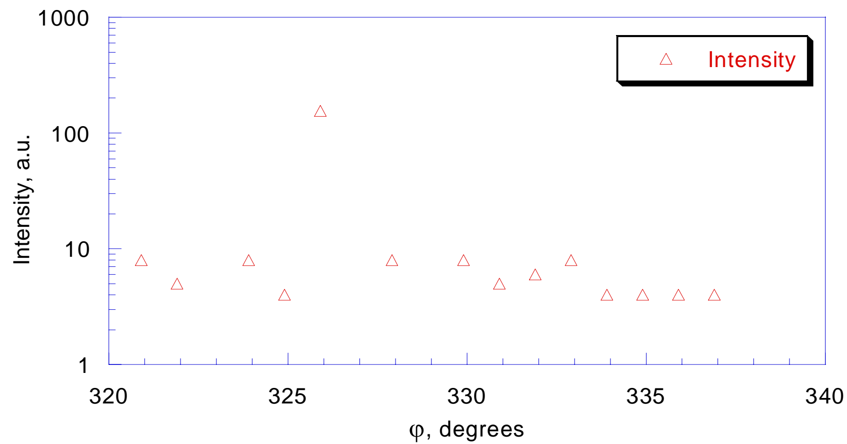

Figure 24. Azimuth scan at ω_s=50.75˚; 1˚ step

The values of the maximum intensity and the corresponding sample position φ are 155 and 325.90˚, respectively.

8. Accurate determination of the φ sample position at the fixed ω_S with the step of 0.5˚ (Figure 25). Searching the position within the ±1˚ range of the φ value found in the previous step.

المنارة للاستشارات
www.manaraa.com

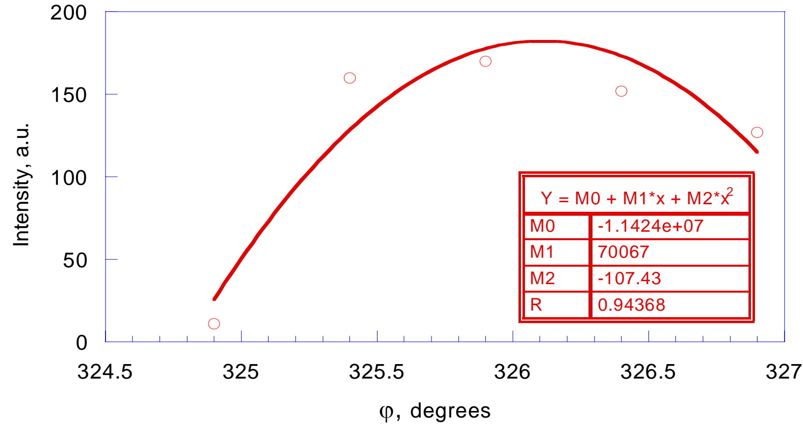

Figure 25. Azimuth scan at ω_S=50.75˚; 0.5˚ step

The polynomial fit curve shows the value of φ corresponding to the maximum intensity. Calculation of the φ position is carried out using the center of mass method:

$$R = \frac{\sum m_i r_i}{m_i}. \tag{25}$$

The calculated value of φ is equal to 326.10˚ and is corresponding to the maximum intensity of 170 photons/sec.

9. Accurate positioning of the sample at the ω_s angle. Measuring the X-ray intensity for 90 seconds and determination of the peak position as 2θ (Figure 26).

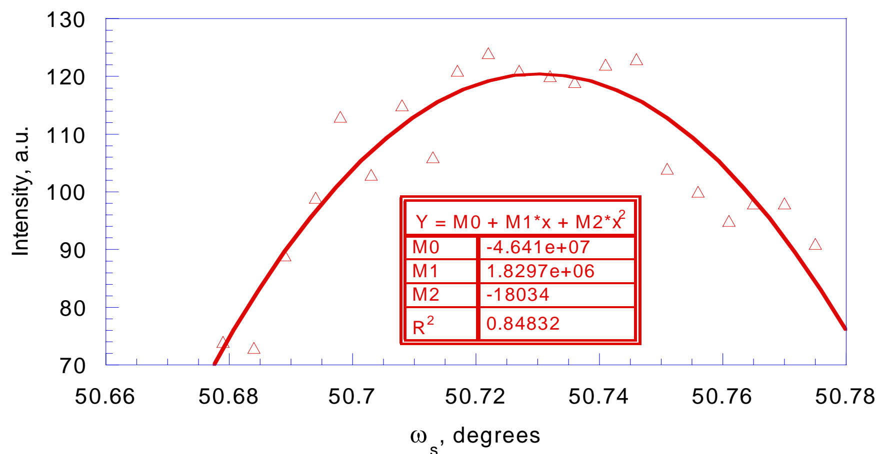

Figure 26. Omega (ω_S) scan at the maximum intensity; 0.005˚ step

المنارة للاستشارات
www.manaraa.com

The polynomial fit curve shows the value of ω_s, which corresponds to the maximum intensity. Using the center of mass method (20), the ω_s position of the sample corresponding to the maximum intensity is at 50.7322˚. The actual maximum intensity registered during the scan is 124 photons/sec.

The results obtained from the measurement process are shown in Table 3.

Table 3. Final experimental results

Specimen position (ω)	50.732˚
Detector position	162.501˚
Maximum intensity	124 photons/sec
Peak relative position	-4.115˚
Peak absolute position (2θ)	158.386˚
Theta (θ)	79.193˚
Lattice constant (a)	4.407281 Å

المنارة للاستشارات
www.manaraa.com

Chapter 7

Summary and Future Work

7.1 Summary

Today, with the increasing interest of designing more efficient engines and turbines, improving their performance, the accurate measurements of high temperatures become more demanding. Neutron irradiation and the X-ray diffraction analysis of the single crystals 3C-SiC turns them to the Maximum Temperature Crystal Sensors (MTCS) enabling to measure the maximum temperatures. The sensors' small size, weight and capability of measuring the high temperatures in hard to access places make them attractive for many applications. Moreover, a wide measuring temperature range of the MTCS sensors (100 – 1400 ˚C) along with their unique physical and chemical properties makes them applicable in almost any environment.

In order to determine the crystal lattice parameter of 3C-SiC, the adjustment and precision alignment procedures of the DSO-1M X-ray diffractometer were developed. The methodology of the neutron irradiated 3C-SiC lattice parameter was described by the X-ray diffraction analysis enabling one to determine the maximum temperature of the MTCS sensor.

www.manaraa.com

Table 4. Brief characteristics of temperature measurements methods in hard to access places

Type measurement category, characteristics	Applicable device	Operation	Advantages	Disadvantages
Contact readout methods provide continuous measurements at stationary and transient regimes; possible automation; output readout mechanism is necessary.	Resistance sensors	Electrical resistivity as a function of temperature	High accuracy of measurements, wide measurement range	Averaging-out of temperature over the length of a sensor
	Thin-film resistance sensors		No temperature distortion	Averaging-out of temperature of a sensor, low stability. Film thickness prop. dependence
	Thermocouples	Voltage at the welding joint as a function of temperature	High accuracy of measurements, wide measurement range	Size of a sensor, temperature distortion of tested parts
	Micro thermocouples		Relatively small size, wide measurement range, high accuracy	Not applicable for micro parts
	Single and twin-lead high temperature thin-film resistance sensors		Applicable for micro parts temperature measurements	Temperature measurement distortion due to a voltage at the welding joint
Non-contact readout methods provide measurements where the contact readout methods are not applicable; maximum temperature measurements only; readings are possible to obtain after the test is completed only	Fusible metal thermo-couples	Melting of metal plugs	Simplicity of readings decoding	Size, discontinuity of readings
	Thermal paints	Thermal paint color or its conditions change with temperature	Part's integrity	Discontinuity of readings, subjectivity of color change estimation
	Thermoplugs	Steel hardness as a function of temperature and exposure time	Relatively small size	High complicity of production of a big set of plugs with equal properties, exposure time data is necessary
	Radioactive tracers	Dependence of the tracer's discharge speed from the tested part on temperature	No changes in physical or chemical properties of tested parts	High complicity of saturation of the tested part with radioactive tracer, complicity if readings decoding
	MTCS	Dependence of crystal lattice parameter of the irradiated crystal on temperature and exposure time.	High accuracy of measurements, wide measurement range, small size	Exposure time data is necessary

المنارة للاستشارات
www.manaraa.com

7.2 Future work

Small sensor's size, its wide range of measured temperatures and high accuracy makes MTCS widely used in many applications. However, the MTCS method requires some improvements. First of all, it is the temperature measuring range which is limited by the temperature of 1400 ˚C for 3C-SiC based MTCSs.

Increasing the temperature range of 3C-SiC sensor towards the higher temperatures is limited by the fact that the majority of defects are annealed prior the temperature reaching 1400 ˚C. The following increase of temperature causes annealing of a small portion of defects only. This phenomenon negatively affects the accuracy of temperature measurements.

One of the other materials suggested for high temperature measurements is an unannealed graphite [5]. Its lattice parameter is considerably larger than for the annealed graphite and depends on the annealing temperature. The higher the temperature, the smaller lattice parameter is. While a crystal lattice change of 3C-SiC is almost negligible in the high temperature range, a lattice parameter change of graphite is at its maximum. Realization of this method is facing some obstacles due to a low chemical stability of graphite and a low accuracy of temperature measurements. The error can reach ±50 ˚C due to inaccurate determination of the lattice parameter of unannealed graphite measured with the diffractometer method [5].

Increase of a higher level of the measured temperature range also assumes finding new materials where defects are annealed at higher temperatures than for 3C-SiC or diamond. At this point, it would be interesting to investigate behaviors of beryllium oxide with its melting temperature of 2530 ˚C and a high thermal conductivity. Another material that would be interesting to examine is a cubic modification of boron nitride. It is known that the boron nitride can exist as various polymorphic forms, one of which is analogous to diamond and one analogous to graphite. These features make it an attractive material as a possible alternative to 3C-SiC and diamond.

MTCS, investigated in the current work, have been irradiated in a nuclear reactor at 100 ˚C. This temperature determines a lower level of the temperature range measured

المنارة للاستشارات
www.manaraa.com

with MTCS. At some nuclear reactors, it is possible to irradiate materials at lower temperatures. Thus, the defects will start to recombine at the lower irradiation temperatures, thereby increasing the temperature range towards the low temperatures. However, it has been experimentally proved that a lower temperature limit cannot be less than 50 ˚C [5], [23]. Experiments showed that a 3C-SiC crystal lattice does not change much at the irradiation temperatures starting from the room temperature up to 100 ˚C. It can be seen from a plot in Figure 27 obtained from data collected in [23]. A 50 ˚C lower limit of the temperatures measured with MTCS has a significant importance as some of the devices operate at the temperature range from a room temperature to 100 ˚C. At the same time, such a temperature range brings a restriction for storing the sensors as they have to be kept at low temperatures to avoid undesirable annealing of defects prior to testing.

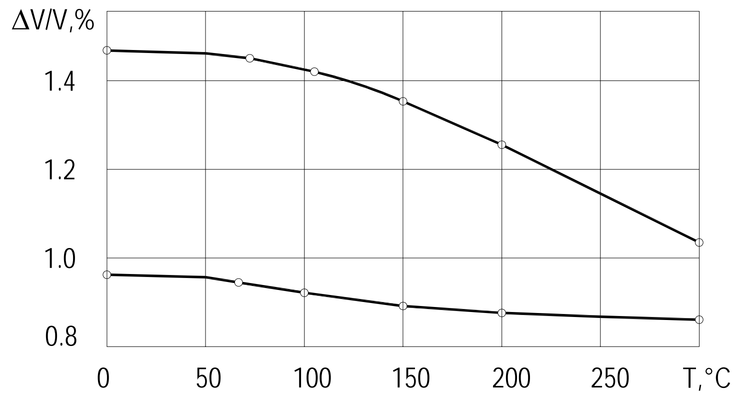

Figure 27. Isochronous annealing of diamond and 3C-SiC irradiated at the temperature of 196 ˚C and stored at 0 ˚C [5]

Broadening of a range of exposure time during tests may be achieved by increasing the exposure time while calibration of MTCS. However, prolongation of the exposure time experiences some difficulties due to a complexity of maintaining a fixed temperature for a long period of time.

Many experiments require a short exposure time of less than 100 seconds. Such a short exposure time is usually followed by a rapid heating that may cause sensor overheating. Defects created by neutron irradiation that cause crystal lattice expansion of

المنارة للاستشارات
www.manaraa.com

3C-SiC have an excess energy of 2 MJ/kg. Heat created by annealed defects during rapid temperature increase, can not be efficiently removed from the sensor. It causes overheating of 3C-SiC to the temperatures higher then the actual measured temperature. As a result, readings obtained from the overheated MTCS are significantly overestimated. In order reduce the energy release at high heating rates, MTCS has to be preliminarily annealed at the temperature of 100 – 200 ˚C less then expected temperature during the test. A heating rate during annealing should not exceed 200 ˚C/sec, while the exposure time cannot be much larger than the expected time for the following test. At this, a significant portion of the stored energy can be released from 3C-SiC.

Besides a lattice parameter change, other materials properties may be considered for temperature indication, such as electro or thermo conductivity change.

المنارة للاستشارات
www.manaraa.com

References

1. D.F. Simbirsky, “*Temperature diagnostics of engines”*, Technics, 208 (1976)

2. J.I. Bramman, A.S. Fraser, W.H. Martin, International Conference on Fastreactor Irradiation Testing, 14 (1969)

3. Templug User Information Guide, Testing-Engineers, Inc., Rev.2.0, 1997

4. A.N. Gordov, A.S. Arzhanov, V.Y. Bilyk et al., “*Temperature measurement techniques in industry”*, 432 (1952)

5. V. A. Nickolaenko, V. I. Karpukhin, “*Temperature Measurements by means of irradiated materials”*, Energoatomizdat, 35, 117 (1986)

6. Thermal Paint Technical Information, Rolls-Royce Inc., (www.rolls-roice.com)

7. A. Guiner and G. Tennevin, Acta Cryst., 2,133 (1949)

8. A.A. Volinsky, L. Ginzbursky. “*Irradiated Cubic Single Crystal SiC as a High Temperature Sensor”*, Mat. Res. Soc. Symp. Proc. Vol. 792, R5.3 (2003)

9. V.A. Nikolaenko, V.A. Morozov, Russian Research Center “Kurchatov Institute”, Moscow, Russia V.P. Timoshenko Molniya-T, Moscow, Russia

10. A.A. Volinsky, V. Timoshenko, V. Nikolaenko, V. Morozov. “*Irradiated Single Crystals for High Temperature Measurements in Space Applications”*, Mat. Res. Soc. Solid State Phenomena, Vols. 108-109, 671-676 (2005)

11. R. Devanathan, W.J. Weber, J. Nucl. Mater, 258, 278 (2000)

12. R. Devanathan, W.J. Weber, F. Gao, J. Appl. Phys, 90 (2001)

13. H. Heinisch, L.R. Greenwood, W.J. Weber, R.E. Willi-ford, J. Nucl. Mater. 307–311 (2002)

www.manaraa.com

14. J. M. Perlado, L. Malerba, and T. Diaz de la Rubia, Mater. Res. Soc. Symp. Proc. 540, 171 (1999)

15. V. A. Nickolaenko, V. I. Karpukhin, S. I. Alekseev, I. D. Konozenko, "*Physics of Radiation of non-metallic crystals*", Naykova dymka, 322-329 (1971)

16. V. I. Karpukhin, O. K. Chugunov, "*Reactor's γ-irradiation and its influence on annealing of defecs*", 38 (1949)

17. V. A. Nickolaenko, V. G. Gordeev, M. I. Baneeva, "*Super hard materials*", 15-19 (1983)

18. E. R. Vance, J. Phys, Solid State Phys, 257-262 (1971)

19. A. Damask, G. Jeans, "*Point defects in materials*", 17-26 (1966)

20. S. T. Konobeevsky, "*Irradiation effect on materials*", 201 (1967)

21. V. A. Nickolaenko, International conference summary, *"Radiation physics of semiconductors and relative materials"*, (1987)

22. J.R. Saltvold, "*A survey of temperature measurement*", Atomic Energy of Canada Limited, AECL, 51 (1976)

23. V.M. Koshkin, Y.A. Frayman, L.P. Galchinezky, "*Physics of Solids*", 212-214 (1977)

24. A. Guiner and G. Tennevin. "*Progress in Metal Physics*", 2, 177 (New-York: Interscience, 1950)

25. B.D. Cullity. "*Elements of X-ray diffraction, second edition*", by. Department of Metallurgical Engineering and Materials Science, University of Notre Dame, (1978)

26. Craig R. Barrett, William D. Nix, Alan S. Tetelman. "*The principles of Engineering Materials*". Department of Materials Science and Engineering, Stanford University; Materials Department, University of California. 56 (1978)

27. H. Huang, N. Ghoniem, J. of Nuclear Mater. 250, 192-199 (1997)

المنارة للاستشارات
www.manaraa.com

28. W.J. Weber, F. Gao, R. Devanathan, W. Jiang, Y. Zhang, "Experimental and *Computational Studies of Ion-Solid Interactions in Silicon Carbide"*, Mater. Res. Symp. Proc., Vol. 792 R5.1 (2004)

29. A.A. Volinsky, L.G. Ginzbursky, V.A. Morozov, *"Crystal Temperature Sensor Technology Status and Future Research"*, 2003 ASME Mechanics and Materials Conference book abstracts. June 2003, Scottsdale AZ, 10 (2003)

30. V.N. Kuznetcov, V.A. Nikolaenko, *"Maximum Temperature Measurement Metrology by means of MTCS"*, Institute of Atomic Energy by I.V.Kurchatov (1979)

31. G. Borrmann. *"Physik Z."*, 42, 157 (1941)

32. N.V. Smirnov, I.V. Dunin-Barkovsky, Probability and Statistical Methods in Technical Applications, "Science", (1969)

33. B.S. Dubov, N.M. Kopytin, "Measuring techniques", Vol.12, 70 (1969)

المنارة للاستشارات
www.manaraa.com

Appendices

المنارة للاستشارات

www.manaraa.com

Appendix A. DSO-1M X-ray diffractometer description

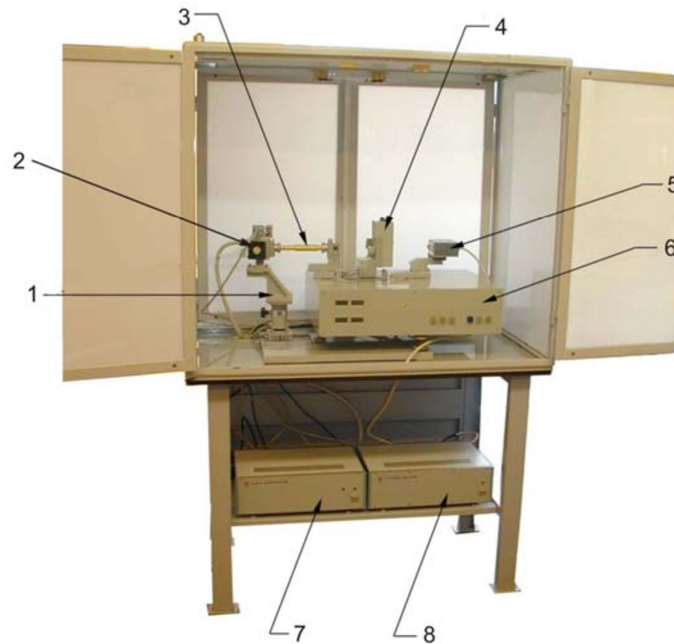

Figure A1. DSO-1M diffractometer

The diffractometer DSO-1M is produced by Radicon Ltd. (Saint-Petersburg, Russia) and includes the following major components: 1 – adjustable column; 2 – X-ray source unit; 3 – collimator tube; 4 – sample holder; 5 – detector; 6 – goniometer; 7 – X-ray generator; 8 – control block.

The diffractometer is designed for determination the orientation of single crystals 3C-SiC and calculation the crystal lattice parameters. The 2θ angle range is 0º-168º. The angle measurement accuracy is ±0.01º. The X-ray source is *Fe-Kα* with the wave length of 1.936 Å. The diffractometer is equipped with the position-sensitive detector which is capable of registering the X-rays with the wave length within the 1.0 Å - 2.5 Å range.

The goniometer provides the ω rotation (Figure 21) of the sample in the range of 0° - 360° with the error of 0.005°; the φ rotatation of the sample is in the range of 0° - 360° with the error of 0.02°.

المنارة للاستشارات
www.manaraa.com

Appendix B. Radicon Device Programming Workbench

Radicon Device Programming Workbench (RDPW) is an application software for IBM-clone personal computers aimed to program and automate the operation of various hardware components of X-ray diffractometer's position-sensitive detectors, motors, relays and angular encoders.

RDPW main shell is hardware independent. All specific hardware-dependent functions are provided by installable device drivers. Apart from RDPW the device drivers provide the manual control of device operations. For each part of the system a separate interactive control window is provided. RDPW integrates various device drivers in a unique system and enables the user to automate all the operations. In addition, RDPW provides programmable data acquisition as well as monitoring of system operation both in text and graphic representation. RDPW offers flexible user interface, including standard file and edit operations, compilation and execution of user programs written in Radicon Device Programming Language (RDPL).

The control block is assembled in euro-standard 19" 3U racks and connected to the computer via an RS-232 port. The control block has a control card with a microprocessor and power supplies on board. It allows operating two stepping motors, two couplings, two angular encoders, a shutter, position-sensitive detector, high voltage generator and limit stops.

B.1 Speed bar

The RDPW speed bar provides shortcuts for the commands <File>, <View>, and <Run> menu (Figure B1). The speed bar has help hints which display a small pop-up window containing the name or brief description of the button when the cursor is over the button for longer than one second.

Figure B1. RDPW Speed bar

المنارة للاستشارات
www.manaraa.com

B.2 Installable Device Drivers

Installable Device Driver (IDD) represents a linkable module that provides full hardware control. IDD is a dynamic link library, which exports the set of predefined functions. These functions provide all necessary information about hardware that this IDD supports, such as names and types of objects, their parameters and functions.

B.3 Radicon hardware server window

The Radicon hardware server window contains collection of command buttons, labeled with device system names (Figure B2).

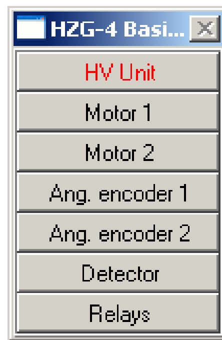

Figure B2. Radicon hardware server window

Radicon hardware server provides several types control windows aimed to operate the devices of appropriate type. The control windows are:

1. Controller;
2. HV Unit;
3. Motor window;
4. Angular encoder window;

المنارة للاستشارات
www.manaraa.com

5. Detector window;
6. Relays window.

B.3.1 Controller window

The Controller window is opened by selecting the <Hardware Connection…> button in the Radicon Server window (Figure B3). The Controller window allows to choose the RS-232 port for connection with a computer. A green color in the window indicates that a device is connected to a computer successively and is ready for work. Any mistake in connection is shown with a red color indicator.

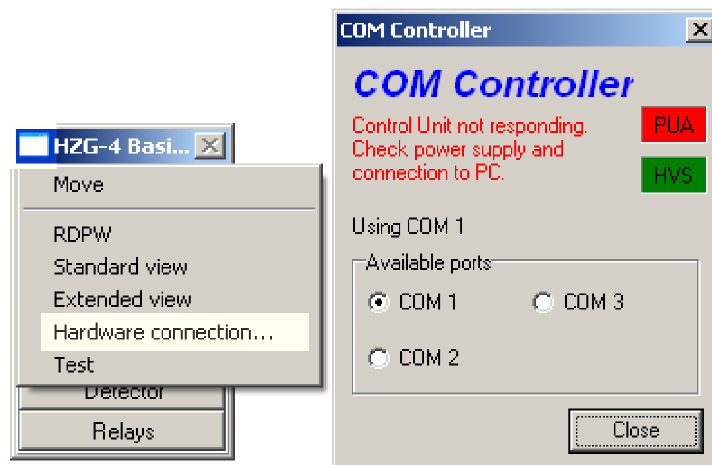

Figure B3. Controller window

المنارة للاستشارات
www.manaraa.com

B.3.2 High voltage unit window

The High voltage unit window allows controlling and setting the high voltage and anode current of the X-ray tube (Figure B4). The high voltage range is 15 kV - 45 kV, the tube current range is from 0.2 mA - 5 mA. The limit power of X-ray tube is 75 watts. The product of high voltage by current should not exceed this limit power.

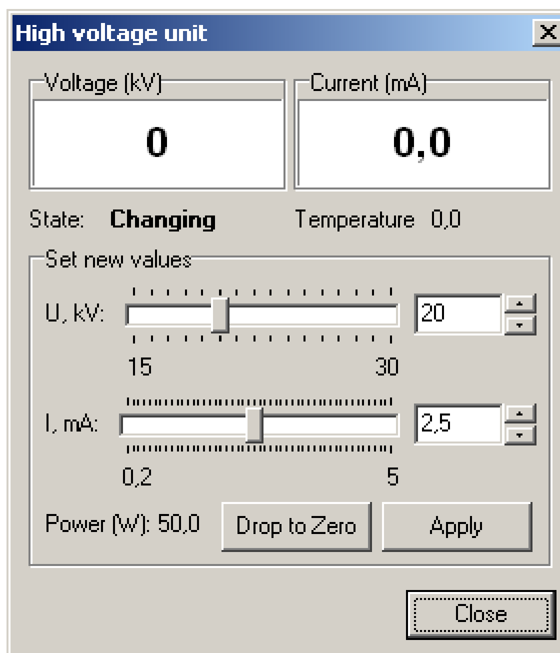

Figure B4. High voltage unit window

B.3.3 Motor window

The current status of the motor, its position and status of the motor's limit stops are shown on the top of the Motor window (Figure B5). The operation block includes the commands controlling the motor. The first row of the buttons <Back> and <Forward> rotate the motor at the angle specified in the field in between. The angle is taken

المنارة للاستشارات
www.manaraa.com

relatively to the current position. The next row of two buttons <Back> and <Forward> serves for continuous rotation of the motor to one of the selected directions.

Figure B5. Motor window

When one of these buttons is pressed, the motor starts to rotate at the selected direction continuously or until its driven element reaches one of the limit stops. The lower row of buttons is responsible for stopping and turning off the motor. In order to stop the motor in the normal regime, the button <Stop> has to be pressed. If it is necessary to stop the motor instantly, press the button <Emergency abort>. The <Loose> button relieves a stress at the motor due to the emergency stop.

One motor (Motor 1) can move both, the position-sensitive detector and the sample holder depending on the coupling position. The coupling position is selected from the Relays window (Figure C2).

المنارة للاستشارات
www.manaraa.com

B.3.4 Power transmission of the step motor

Three tabs in the bottom of the Motor window show the parameters of power transmission, acceleration parameters of the motor and the operational currents of the motor (Figure B6).

Figure B6. Mechanic tab; motor window section capture

There two options that can be adjusted in the Mechanic tab are the number of steps per turn and the gear ratio. Both motors installed in the diffractometer DSO-1M have the rate of 200 steps per revolution. The first gear ratio number is a number of cogs of the driven gear wheel; the second is a number of cogs of the driving gear wheel, which is rotating with the motor's spindle. The gear ratios used in DSO-1M are shown in Table B1.

Table B1. Motor's gear ratios

Gear	Gear ratio
Position-sensitive detector	1500:1
Sample holder	3000:1
Azimuth rotation	90:1

In order to change and save the settings the button <Apply> has to be pressed. To restore the settings after the accidental change, press the button <Restore>.

www.manaraa.com

B.3.5 Speed of rotation of the step motor

The second tab in the bottom of the Motor window shows the frequency settings of the motor (Figure B7).

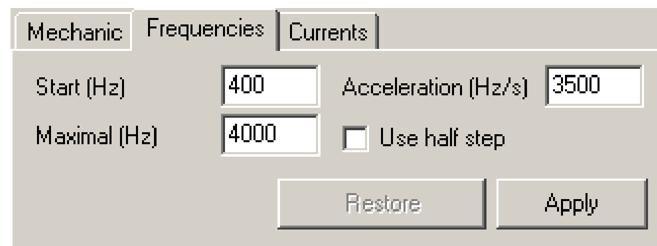

Figure B7. Frequencies tab; motor window section capture

The motor cannot start with the high frequency rotation, so it accelerates with time. The maximum frequency of rotation is also limited by the motors mechanical features. Furthermore, the motors have the resonant speeds at which they can work during acceleration only.

The field <Start> shows a starting frequency of rotation of the motor (Hz). The field <Maximal> shows a maximum frequency of rotation of the motor (Hz); the frequency rises to the maximum chosen frequency and the motor starts rotating at this frequency continuously. The field <Acceleration> shows a value of acceleration (Hz/sec).

Practically, the frequency value represents a number of steps made by the motor per second.

The Half step regime reduces the number of steps of the motor per impulse by half, while at the regime of a full step one impulse corresponds to one step. In that way the motor which makes 200 steps per one revolution at the frequency of 600 Hz will rotate at the speed of 3 rev/sec in the full step regime or 1.5 rev/sec in the half step regime. The values of frequency recommended for the motors are shown in Table B2.

المنارة للاستشارات
www.manaraa.com

Table B2. Recommended frequency values for motors

Motor 1 (SM1)	400 – 4000 Hz
Motor 2 (SM2)	450 – 3500 Hz, resonance frequency range: 700 – 2500 Hz

B.3.6 Operation points of the step motor

The last tab in the bottom of the Motor window shows the settings for the motor's operation points (Figure B8).

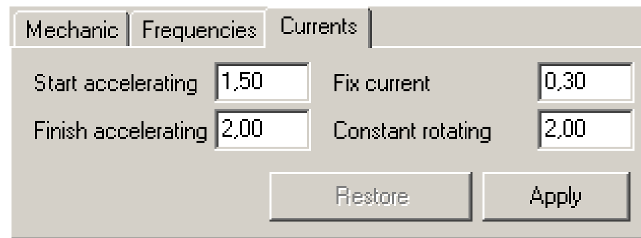

Figure B8. Motor's operation points; motor window section capture

A change of the current with time at different operational points are shown schematically in Figure B9.

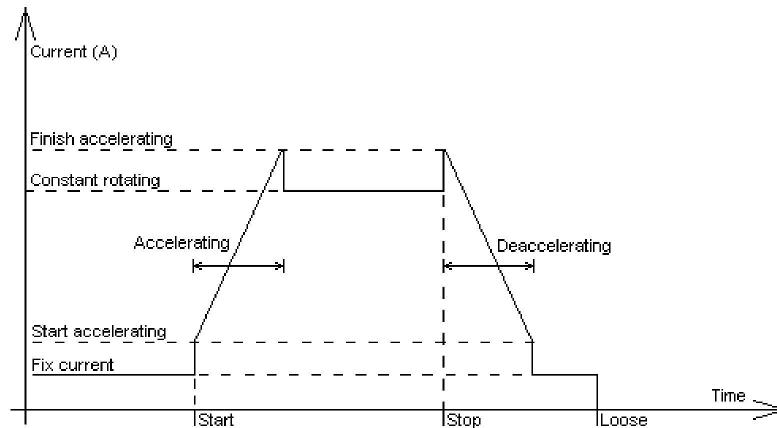

Figure B9. Motor's operation points scheme

المنارة للاستشارات
www.manaraa.com

The scheme shows how the value of current changes in different motor's operation modes. At the working mode the motor is supplied with the Fix Current that is enough only to keep the motor in current position. When the command Start is launched, the current value jumps to the Start acceleration current value producing the stepping impulses in the motor. The motor starts accelerating with time and the current value rises linearly to the value of Finish accelerating current. When the maximum rotation frequency is reached, the motor switches to the mode of continuous rotation. At the same time the current jumps down to the value of Constant rotating current. Before reaching the stop point, the motor slows down in order to stop completely at the specified position. A deceleration process is in a reverse order of the acceleration process. First, the current value jumps up to the Finishing accelerating current value and then linearly decreases to the Start acceleration current value. When the motor is stopped, the current value drops down to the value of the Fix current. The command Loose relieves a stress at the motor due to a stop.

B.4 Angle encoder window

The optical angle encoders are used to control the positions of both the position-sensitive detector and the sample holder. The sample holder is controlled by the Angle Encoder 1, while the position-sensitive detector is controlled by the Angle Encoder 2. The operation window for the Angle Encoders is shown in Figure B10. The position of the angle encoders is shown in the top right corner of the Angle encoder window. The Settings block shows the mechanical settings for the encoder. "Discrets per turn" means a number of counts per one revolution of the position-sensitive detector. Both angle encoders have 4000 counts per revolution. The reverse option indicates that the direction for positive counting of the angle is opposite to the positive direction of the encoder rotation.

المنارة للاستشارات
www.manaraa.com

Appendix B (Continued)

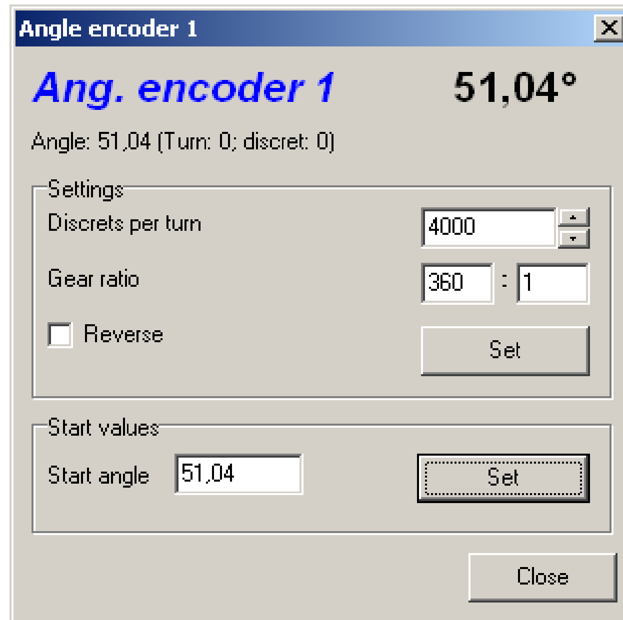

Figure B10. Angle encoder window

The gear ratios used in DSO-1M for the sample holder and the detector are shown in Table B3.

Table B3. Encoder's gear ratios

	Name	Gear ratio	Reverse
Sample holder	AE1	360:1	No
Detector	AE2	360:1	Yes

In order to input new setting for the sensor press the button <Set> in the Settings block. Then it is necessary to run the sensor for one turn.

The block Start values initialize the sensor by its current position. Enter a value of the angle in the field Start and press the button <Set> in the Start values block.

المنارة للاستشارات
www.manaraa.com

B.4.1 Position-sensitive detector window

The position-sensitive detector window shows the parameters of the position-sensitive detector. The window has two tabs: Spectrum and Calibration (Figure B11).

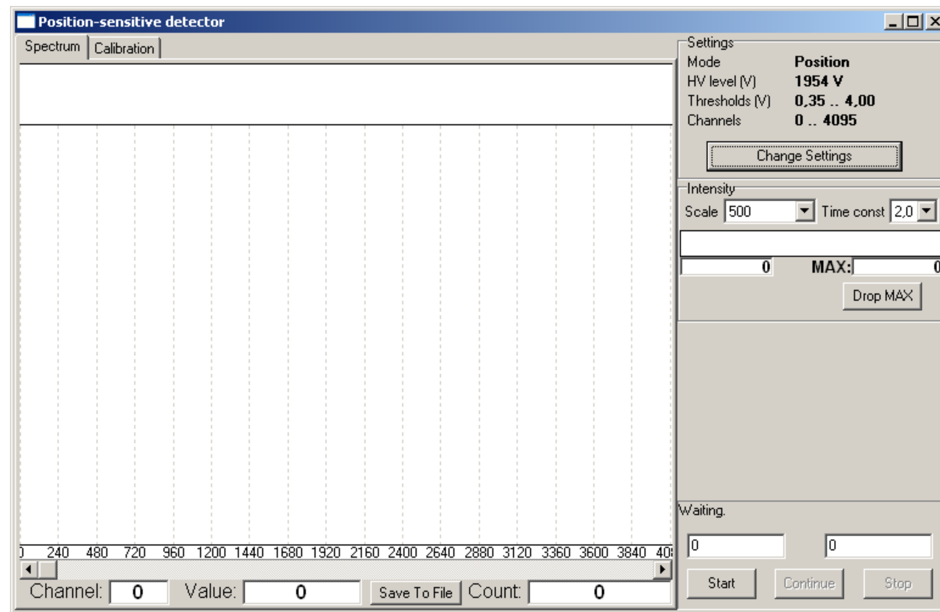

Figure B11. Position-sensitive detector window

The most part of the window shows a distribution of the intensity registered by the position-sensitive detector. The current settings of the position-sensitive detector are shown in the right top corner of the window. The settings can be changed by clicking the button <Change Settings>.

The Intensity block shows a current intensity of X-ray radiation. The intensity is presented by a red color horizontal stripe. Both the maximum and the current intensity are shown in a numerical form in the fields below the stripe. The <Drop MAX> button resets a value of the maximum intensity.

المنارة للاستشارات
www.manaraa.com

The position-sensitive detector is controlled by the buttons located in the right bottom corner of the detector's window. There are two data fields above the controlling buttons. The data filed on the left counts the time since starting the intensity measurement. The data field on the right is the input field where the time of measurement has to be entered in seconds. If the time of measurement entered in this field is zero, the position-sensitive detector will be working until the operator stops it with the button <Stop>.

In order to start the measurement of intensity, click the <Start> button. The position-sensitive detector will be measuring the intensity of the X-ray radiation for the time entered in the right bottom input field. The measurement can be stopped with the button <Stop> and resumed with the button <Continue>.

The measured intensity is presented in the form of a spectrum. The upper field of the position-sensitive detector window shows a map of the spectrum, while the large part of the window shows the current section of the spectrum. The value of intensity in a channel can be seen by clicking on the channel of the spectrum. A scale of the spectrum can be changed by holding the button <Ctrl> on the keyboard and left/right clicking on the selected part of the spectrum.

The channel mode, its value and the total number of counts are shown in the fields below the spectrum image.

B.4.2 Settings of the position-sensitive detector

The work regime of the position-sensitive detector can be selected in the "Analyse mode" box in the detector settings window (Figure B12). There are two modes available: the amplitude mode and the position mode. In the amplitude mode, the power distribution is registered by the registered photons, while the position mode registers the places of the detector where the interaction with the photons occurred.

www.manaraa.com

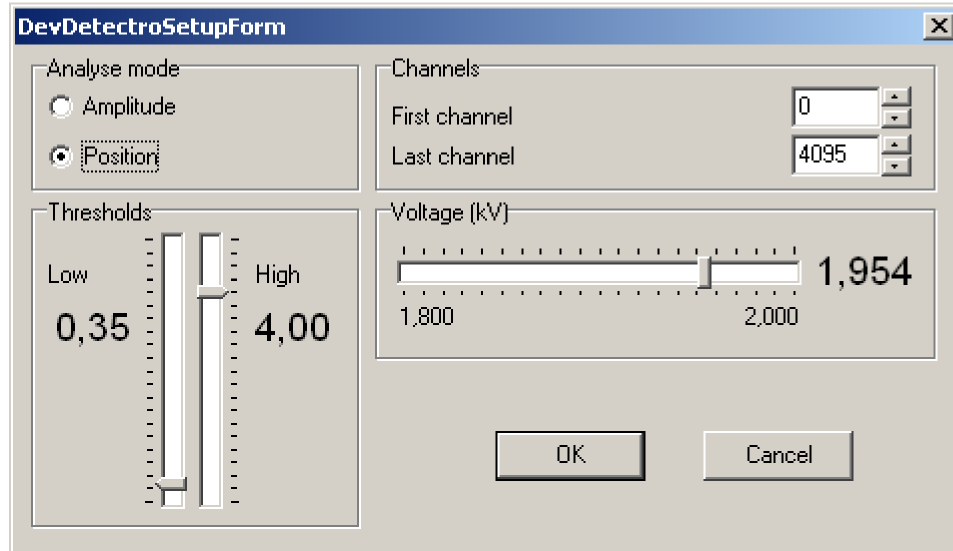

Figure B12. Settings window of position-sensitive detector

The first and the last channel values define the range of the detector's operational channels. There are 4096 channels in the position-sensitive detector. However, the outermost channels are not usually used as they register the apparatus background noise only.

Thresholds value defines the energy range registered by the position-sensitive detector. The voltage bar defines the current value for the position-sensitive detector in kV. The voltage has to be set up at the value when the intensity maximum value (peak) corresponds to the channel's value of approximately 500.

The next tab represents the calibration function of the position-sensitive detector (Figure B13). The calibration tab is used for plotting a calibration curve of the channel as a function of the detector's position angle. The calibration procedure is described in the Appendix C.3.

المنارة للاستشارات
www.manaraa.com

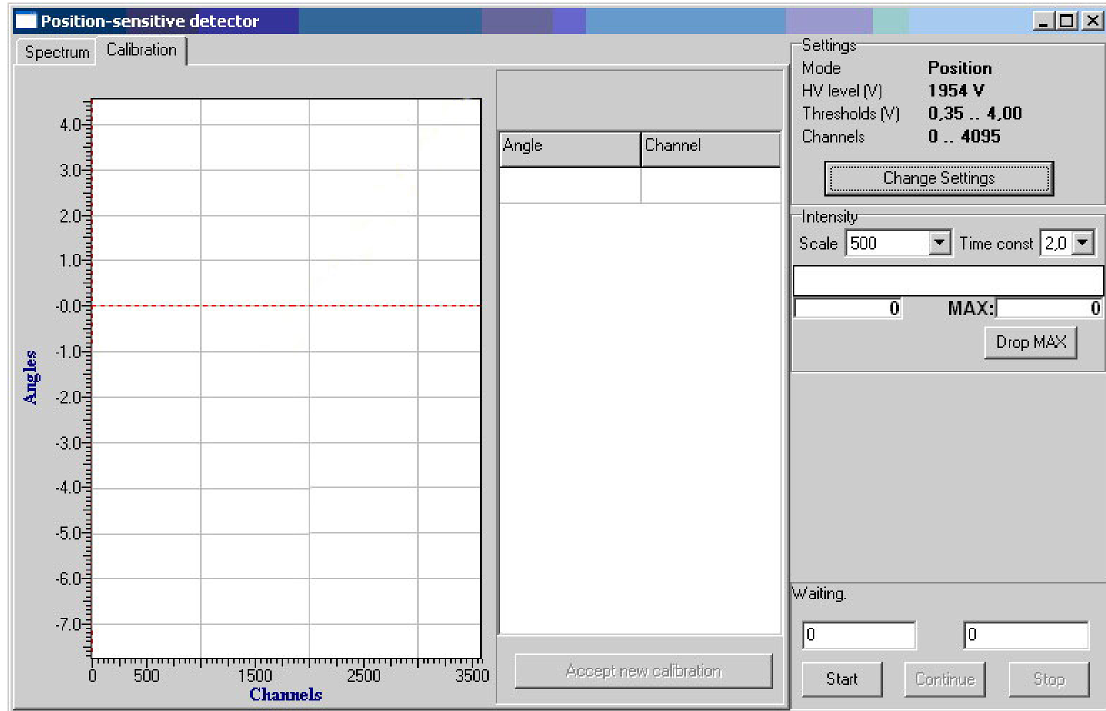

Figure B13. Calibration tab; position-sensitive detector window

B.5 Relays window

All the relay elements are shown in Figure B14: the shutter, the position-sensitive detector and the sample holder (specimen).

Each element has a reserved designation RS0…RS3 used by macro commands. By clicking the buttons on the right, the elements switch their regime to the On/Off mode. The elements names may be changed by clicking the button <Change names>. The elements with the reserved name RS0 is not used for the diffractometer DSO-1M.

المنارة للاستشارات
www.manaraa.com

Appendix B (Continued)

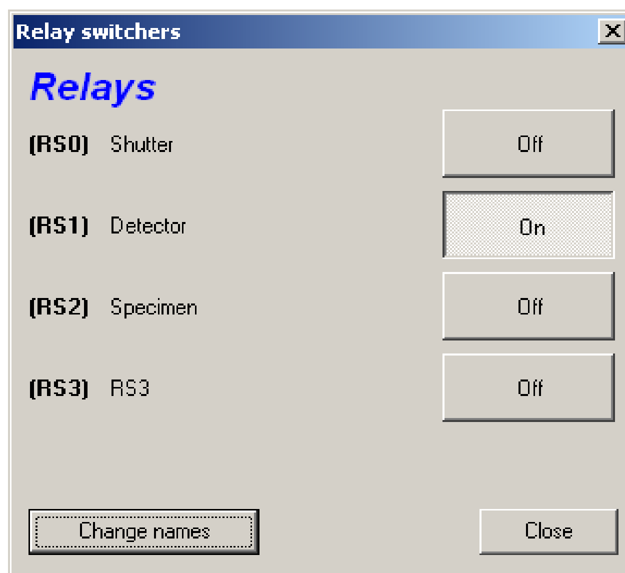

Figure B14. Relays window

المنارة للاستشارات
www.manaraa.com

Appendix C. DSO-1M operation manual

C.1 Mechanical initialization

When all the units are assembled, all cables are connected and the software that operates a diffractometer is installed, the device can be turned on. There are three power switches which are located on the goniometer, control block and X-ray generator, respectively. The last two switches are allowed to be kept in the "on" position. The one on the goniometer is a main switch witch turns on the diffractometer and shuts it down.

The next step is initialization. The initialization macro command correlates the readings from both mechanical and optical gauges. It also does a precise positioning of the position-sensitive detector so that it is perpendicular to the X-ray beam. The initialization process is executed using the software "Radicon Device Programming Workbench" (RDPW) with the macro command "Initialize". Prior the initialization it is necessary to remove both a cuvette from a sample holder and a plug from another side of the sample holder. It will allow the X-ray beam to go through the sample holder and be registered by the position-sensitive detector. The plug is made of niobium and designed to minimize a value of a backscattered intensity of the primary beam. The position-sensitive detector is equipped with a damper in the form of a nickel stripe that is recommended to be used during initialization and following calibration with the installed 0.25 mm vertical (SL2) and 0.25 mm horizontal (SL3) slits (Figure C3). With the vertical and horizontal slits of 0.1 m and at the 15kV x 0.2mA regime of X-ray tube power supply, both initialization and calibration can be performed without a damper. The last option is more preferable. A manganese filter F (Figure C3) should be always inserted in order to avoid a damage of the detector.

In the beginning of initialization, an operator will be asked to enter the position readings for both the position-sensitive detector and the sample holder into a window shown in Figure D1. The readings can be found on the mechanical gauges on the face panel of the goniometer (Figure C3).

المنارة للاستشارات
www.manaraa.com

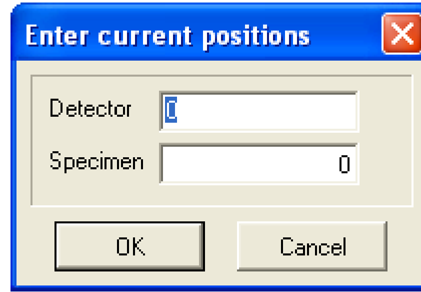

Figure C1. Initial data input window

At the end of initialization, if the X-ray optics scheme of the diffractometer is perfectly aligned, the sample holder and the position-sensitive detector will be located at the normal positions of ω_s=90˚ and ω_d=0˚ respectively. Otherwise, they have to be moved at their normal positions manually using a macro command “Move”. It means that the X-Ray optical scheme of the diffractometer is not adjusted right.

The security lock is located on the back side of the goniometer and should be at the “off” position during initialization and following adjustment procedures. Operations executed by the initialization macro command are:

1. Initialization of optical angle gauges.
2. Moving both the position-sensitive detector and the sample holder to their normal positions perpendicular to the incident X-ray beam.
3. Adjusting the work regime for a high-voltage power supply of the X-ray tube to 15 kV, 0.2 mA voltage and current values, respectively.
4. Opening a shutter for 90 seconds to ramp the intensity of X-ray beam to its maximum and closing the shutter.
5. Locating the position-sensitive detector at the position where its 2048th channel coincides with the center of the peak obtained in the fourth step.

The initialization has to be launched every time when the diffractometer or the controlling RDPW software was shut down.

المنارة للاستشارات
www.manaraa.com

C.2 Instrument alignment

The adjustment procedure consists of aligning of the X-ray optical scheme of the diffractometer. The procedure is necessary after transportation of the device or due to a misalignment of the X-ray optical scheme.

The objective of the alignment is to obtain a narrow X-ray beam passing through the intersection of the axis of the goniometer with the crystal rotation azimuth axis. The next step is to locate a surface of the crystal at the normal measuring position using the X-ray beam. The pre-alignment conditions are shown in Table C1.

Table C1. Pre-alignment conditions

Detector's position	$\omega_d=0^\circ$
Sample holder's position	$\omega_s=90^\circ$
Manganous filter, F	inserted
Slit, SL1	1 mm, horizontal
Slit, SL2	removed
Slit, SL3	0.1 mm, horizontal
Niobium plug	removed
Nickel damper	installed
Sample plate	removed
Security lock	off

In the beginning of the adjustment, start the position-sensitive detector and open the shutter. These commands can be executed with the software RDPW at the main form tab shown in Figure C2. The <Detector> button starts counting the impulses, while the <Shutter> button opens a shutter.

المنارة للاستشارات
www.manaraa.com

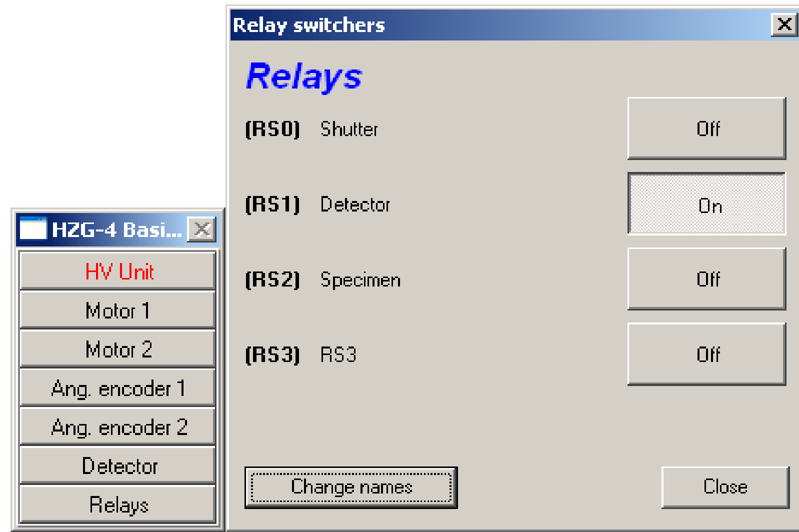

Figure C2. Main form tab and the Relays sub tab

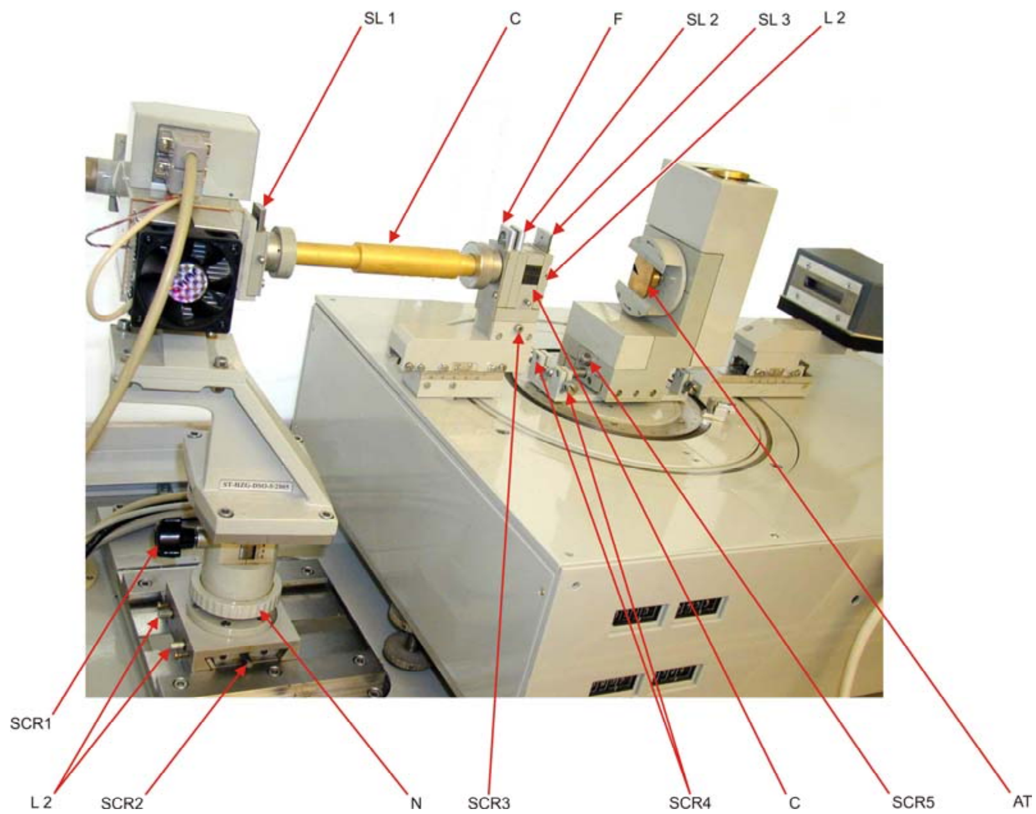

Figure C3. Photo of the measuring unit of the diffractometer DSO-1M

المنارة للاستشارات
www.manaraa.com

At first, the X-ray source position has to be adjusted in the vertical and horizontal directions and rotated at the correct angle about the column supporting the source.

In order to adjust a height of the X-ray source position it is necessary to release the screw SCR1 (Figure C3). After that, the column with the X-ray source, which has two degrees of freedom, needs to be moved up or down using the nut N and manually rotated about its vertical axis. The maximum intensity can be obtained by rotating the nut N clockwise and counter-clockwise as well as moving the column about its vertical axis. For a more precise vertical adjustment of the X-ray source position, it is necessary to use the adjustment tool AT that has to be installed at the sample holder. The tool has a 0.2 mm diameter hole in the center, where the X-ray beam has to be pointed at. By doing the described above manipulations, one can achieve the maximum intensity at the detector. The adjustment tool needs to be installed so that its chamfers are horizontal. The hole has a small displacement (<0.1 mm) outwards the center of the tool. When the maximum intensity at the detector is achieved, the screw SCR1 can be tightened.

The next step is the adjustment of the X-ray source along the direction perpendicular to the X-ray beam. The adjustment tool AT has to be removed and two vertical slits are to be installed; the vertical 0.1 mm and 0.25 mm slits at the positions SL2 and SL3, respectively. The 1 mm vertical slit remains in the position SL1. The locking screws L1 have to be released. Using the screw SCR2 the column can be moved across the X-ray beam direction achieving the maximum intensity at the detector. At the new position of the X-ray source, the screw SCR1 must be released in order to achieve a higher intensity by rotating the column about its vertical axis. After that, it is required to check the existence of the incident X-ray beam in the center of the adjacent tool AT. If the position-sensitive detector is not registering the intensity of the beam, it is necessary to release the locking screws L2 and move the collimator block C until the X-ray beam hits the center of the adjacent tool. The moving of the collimator is possible using the screw SCR3. By replacing the slit SL3 with the 0.1 mm horizontal slit, the vertical adjustment of the X-ray source has to be verified. In order to make sure in the accuracy of

المنارة للاستشارات
www.manaraa.com

the X-ray source positioning relative to the sample holder, it is necessary to move the source gently at all degrees of freedom: across the beam direction, up and down and around the axis of the column. The adjustment is considered to be legitimate if the difference in intensities with the adjacent tool and without one is not higher than 30 – 40 %. After every stage of the adjustment, the locking screws have to be tightened while checking the intensity at the same time.

The final stage of the adjustment is the dividing of the X-ray beam with the adjacent tool AT. It can be done by rotation of the sample holder with the installed adjacent tool at its zero position. At such position, the tool will cut half of the intensity obtained in the previous stage. If the beam did not lose its intensity or lost all of its intensity, then the position of the adjacent tool has to be corrected using the screws SCR4 and SCR5.

C.3 Detector calibration

Prior to the measurement, when the diffractometer is correctly adjusted, it is required to calibrate the position-sensitive detector. It is suggested to warm up the deffractometer for 30 minutes before running the calibration. The procedure of calibration consists in the drawing a scale for the angles of the detector's position relatively to the incident X-ray beam in accordance with the channels of the detector. The center of the detector serves as a base point of the scale.

The calibration process is executed by the macro command "CalibrByRay" from the main form tab or from the drop down menu list in RDPW. An operator will be asked to enter the position readings for both the detector and the sample holder into a window shown in Figure C1. The readings are shown on the mechanical gauges on the face panel of the goniometer. The calibration of the detector needs to be done every month or after

المنارة للاستشارات
www.manaraa.com

replacement of the X-ray tube. The detector has to be calibrated with the nickel damper and the removed niobium plug from the sample holder. The hinged doors must be closed.

The calibration process by the macro command “CalibrByRay” may be described in the following steps:

1. Positioning of the sample and the detector at their initial positions of θ_d=0˚ ω_s=90˚, respectively (Figure 21).
2. Adjusting the work regime for a high-voltage power supply of the X-ray tube to the 15 kV, 0.2 mA voltage and current values, respectively.
3. Measuring the intensity in the center of the position-sensitive detector.
4. Designation of the detector’s edge corresponding to a zero channel (the position-sensitive detector moves to the position of approximately +5˚- +7˚ from its initial ω_d position).
5. Scanning the position-sensitive detector from one edge to another with the 2˚ step. Determination of the correspondence between the angle of the detector’s position relative to the incident X-ray beam and the channel corresponding to the center of a peak. The results may be plotted in the form of a calibration curve shown in Figure C4.

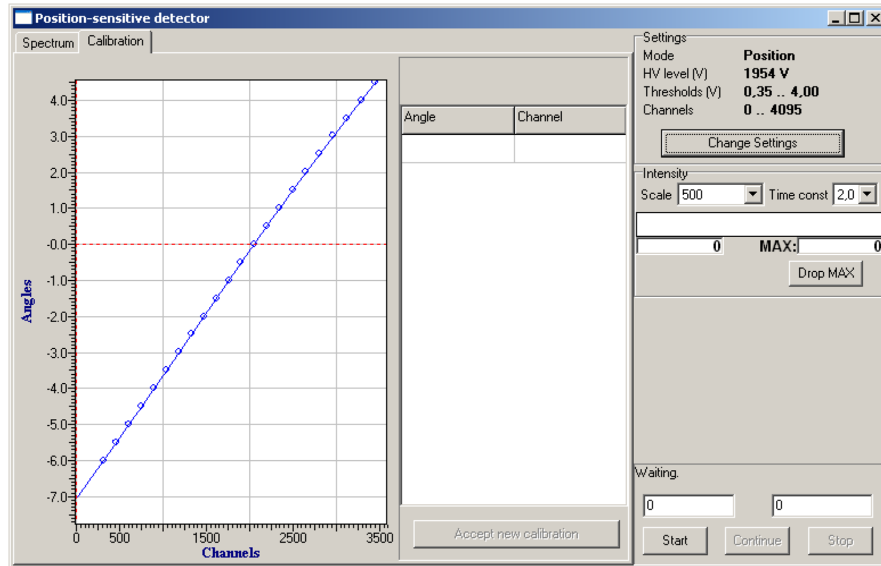

Figure C4. Calibration curve; position-sensitive detector window

المنارة للاستشارات
www.manaraa.com

When the calibration is finished, the hinged doors can be opened. The nickel damper has to be removed from the position-sensitive detector, while the niobium plug is to be installed at the back side of the sample holder. The diffractometer is ready for measurements.

C.4 Crystal lattice parameter measurement

The measuring process is based on the 420 reflection from 3C-SiC crystal lattice and is carried out in a fully automated regime. It is executed by the macro command "Measure" and consists of the finding a maximum intensity of the diffracted beam at the fixed position of the detector at angle $2\theta_d$ and specified scanning θ_s range of the sample. Using the Bragg's law, a crystal lattice parameter of 3C-SiC is calculated from the sample angle θ that corresponds to the found maximum intensity.

The measuring procedure may be described in the following sequence:

1. Activation of the safety switch at the "Lock" position on the back side of the goniometer. During the measurement, the hinged doors of the diffractometer must be closed. If any of the doors are opened, the safety switch blocks the macro command from running.
2. Warming up the diffractometer for 20 minutes.
3. Insertion of the samples. The cuvettes are made of the plastic or plexiglass with the hole drilled in the center. The range of the holes is 0.3-0.6 mm, and designed for different size crystals. If the size of the crystals is relatively different, it is necessary to use the cuvette of the appropriate size. This is important for an accurate centering of the crystal; if the crystal is not centered well in the cuvette, the incident X-ray beam may hit only a part of the crystal. This causes a lowering of the intensity of the diffracted beam, which, in turn, decreases the measurements accuracy. It is recommended to use the technical vaseline for inserting the samples in the cuvettes. However, soft plasticine may

المنارة للاستشارات
www.manaraa.com

also be used using the same installation technique. If the technical vaseline is used, it is required to deposit a small quantity of the vaseline on the inside of the cuvette untill it appears beyond the flat surface of the cuvette. Then the crystal can be placed in the center of the cuvette using a sharp needle. It is recommended to use a microscope or a magnifying lens. After that, the crystal has to be pressed with the polished glass surface or other flat surface plate in order to push the crystal into the hole. It is important that the crystal is inserted flush with the surface of the cuvette; otherwise the error of measurements will be too high. It is also very important to avoid any damages of the cuvette while inserting a crystal as any deformation of the surface of the cuvette will cause additional measurement errors. If the crystal has a quite distinct flat surface, then it is recommended to use this surface in flush with the cuvette's surface in order to decrease a time of finding the wanted diffraction. It also gives the more accurate result.

4. Installation of the cuvette with the crystal in the sample holder. The cuvette with the crystal inside has to be inserted into the bushing in the center of the sample holder and fixed by pushing and rotating the cuvette at 90˚.

5. Closing the hinged doors.

6. Running the macro command "Measure". After launching the command, an operator will be asked to name a sample and specify a measuring mode in the window shown in Figure C5.

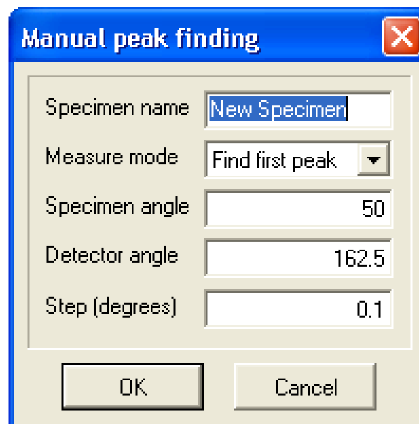

Figure C5. Measurement input data

المنارة للاستشارات
www.manaraa.com

Sample's name would be a name of the log file with the measurement results. The measurement mode can be either to find a diffraction angle of the X-ray beam from the sample or to find the intensity values for a range that can be manually specified. The initial scanning positions for the sample and the position-sensitive detector have to be taken as default, equal to 50˚ and 162.5˚ respectively, with the scanning step of 0.1˚. The position of the center of the detector is fixed and equal to 162.5˚, which corresponds to the angle of $2\theta_d$. During the measurement process, the measurement results can be viewed in the "Log window" opened from the menu "View" of the controlling software RDPW.

7. If the macro command did not finish the measurement and did not give a result, then it is recommended to stop the command and run it again with the smaller initial sample's scanning angle (θ_s=10˚).
8. If the peak still can not be found, it is necessary to reinsert the crystal and repeat the steps described above. It usually takes not more then 30 minutes to find the peak of the intensity diffracted from the crystal.
9. When the measurement is done, the results of the measurement are saved in a file with the name given in step 6.

المنارة للاستشارات
www.manaraa.com

Appendix D. Temperature Measurement Analysis

D.1 Real temperature estimation

A significant portion of systematic error can be excluded using the calibration function (26) [30]:

$$T_{\text{real}} = f_{\text{exp}}(T_{\text{M}}), \tag{26}$$

where T_{real} – is a real temperature; f_{exp} - is an experimental function; T_M - is a value of the temperature measured with MTCS.

The function (26) can be obtained based on the temperature measurements data using both the MTCS and another more accurate temperature measuring device. If the readings of the last device has an error much smaller than that of the MTCS method, the systematic error may be neglected. In this case, the adequacy estimation for calibration function (18) can only be achieved using random uncertainties [30].

The empirical interpretation of the function (26) is based on the MTCS temperature measurement results provided by the research university of Mendeleyev D.I. and Scientific Industrial Union "Termopribor" in Moscow, Russia. The temperature measurement error is 0.2 ˚C and 0.9 ˚C for the temperatures of 100 ˚C and 1000 ˚C, respectively. The temperatures of 100 ˚C and 1000 ˚C are taken as real as the error for these temperatures is very small.

The value of the error δ for every measurement q, is determined as a difference between the temperature measured by the MTCS method $T_{M,q}$, and the real temperature of measurement $T_{real,q}$.

$$\delta_k = T_{M,q} - T_{real,q}. \tag{27}$$

All temperatures measured by the MTCS method and their real values along with the systematic error values, $\Delta_{c,q}$ for every measurement q are given in Table D1.

المنارة للاستشارات
www.manaraa.com

Table D1. Temperature measurements and errors for MTCS at stationary regimes [30]

q	$T_{M,q}$	$T_{real,q}$	δ_q	$\Delta_{c,q}$
1	590	595.8	- 5.8	- 4.97
2	590	598.2	- 8.2	- 4.97
3	590	597.9	- 7.9	- 4.97
4	598	600.0	- 2.0	- 4.97
5	788	798.5	- 10.5	- 4.88
6	793	797.3	- 4.3	- 4.88
7	796	799.0	- 3.0	- 4.88
8	803	799.4	3.6	- 4.87
9	973	981.0	- 8.0	- 4.79
10	982	979.0	3.0	- 4.79
11	996	1000.8	- 4.8	- 4.78
12	1087	1100.7	- 13.7	- 4.74
13	1096	1100.7	- 4.7	- 4.73
14	1103	1100.7	2.3	- 4.73
15	1178	1192.5	- 14.5	- 4.69
16	1190	1198.3	- 8.3	- 4.69
17	1193	1193.3	- 0.3	- 4.69
18	1197	1196.6	0.4	- 4.68

The empirical function (26) can be obtained using regression analysis [21]. The analysis is executed by searching the consistently increasing degree polynomials using the least-squares method. The values of the coefficients of regressions are obtained by comparison of dispersions of the successive approximations using the statistical F-test [32]. As a result of the analysis, a linear function of T_M is obtained:

المنارة للاستشارات
www.manaraa.com

Appendix D (Continued)

$$T = f_{emp}(T_M) = a + b \cdot T_M \,. \tag{28}$$

The values of the conducted analysis are shown in Table D2 [30].

Table D2. Calculated values of linear regression and mean squared deviation of empirical data for MTCS [30]

MTCS type	Linear regression values, degree		Degree of freedom	Mean squared deviation of empirical data, $^oC^2$	
	a	b		ΔR_1	ΔR_2
3C-SiC	5.3	0.9995	16	50.5	27.3

A mean square deviation, ΔR, is obtained from the expressions [30]:

$$\Delta R_1 = \frac{1}{q}\sum_{q=1}^{q}(T_{real,q} - T_{M,q})^2 \,, \tag{29}$$

$$\Delta R_2 = \frac{1}{q}\sum_{q=1}^{q}(T_{real,q} - a - b \cdot T_{M,q})^2 \,. \tag{30}$$

A relative decrease of the ΔR_2 value in comparison with the initial ΔR_1 indicates a preference for using the calibration function, which excludes the systematic error. The value of the excluded systematic error is a linear function of a level of measured temperature:

$$\Delta_{c,k}(T_M) = T_M(1-b) - a \,. \tag{31}$$

www.manaraa.com

The excluded systematic error for 3C-SiC MTCS is approximately -5 ˚C in the temperature range of 600 – 1200 ˚C. The corresponded values of the excluded systematic error $\Delta_{c,k}$, are shown in Table D1 [30].

So, the measurements of the maximum temperature using MTCS can be evaluated with the following equation [30]:

$$T = 5.3 + 0.9995 \cdot T_M \,, \text{ for } 600\ ^\circ\text{C} \le T_M \le 1200\ ^\circ\text{C}. \tag{32}$$

D.2 Statistical measurement error

The residual variance and the standard deviation (SD), σ can be obtained for both the entire and localized subsamples. Using the localized subsamples of volume N_i it is possible to establish a relationship between SD and a measured temperature. The minimum and maximum values of the subsample have been chosen to be equal N_l=2 and N_{max}=15, respectively. Such organization of the subsample excludes the previous data and gradually involves the new ones to the point of excluding all the previous data. A volume of the subsample remains constant at every evaluation.

Using a mean value of T_M in compliance with every subsample makes it possible to find values of the correlating equation (28) for every series i. Thus, the most accurate values of the subsample can be obtained [30]:

$$\frac{\sigma}{T} = \sigma_i(T_M) = \alpha_i + \beta_i \cdot T_M \,, \tag{33}$$

المنارة للاستشارات
www.manaraa.com

where σ_i - is an estimated value of SD; α_i and β_i - are the estimated regression parameters for the i-series. The estimation technique is shown in Figure D1, where q – is a number of experimental data, q = 1, 2, …, Q; i – is a number of subsamples I of different volume, I = 1, 2, …, I. The calculated number J_i of σ (SD) values would be j = 1, 2, …, J_i ($J_i = K - i$) which correlates with a measured temperature. Using the data from Table D1 and Table D2, the plot shown in Figure D1 can be obtained:

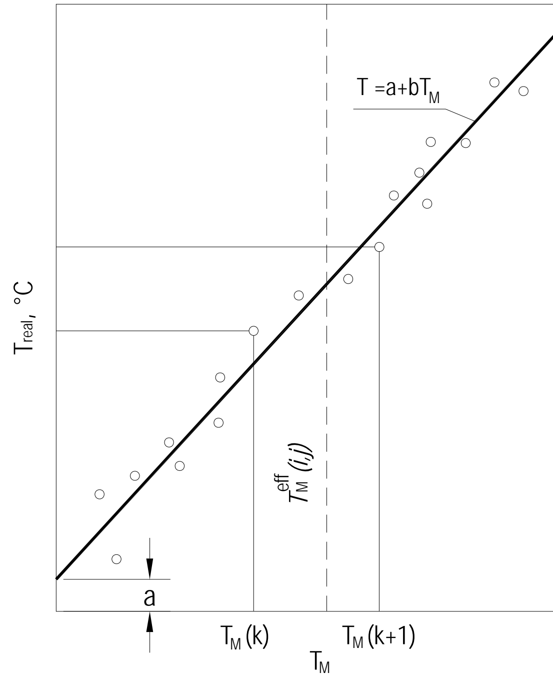

Figure D1. Estimation pattern of σ (SD) as a function of a measured temperature [30]

The measured or effective temperature is a mean temperature of measurements of a subsample. A value of the effective temperature changes with every subsample.

$$T_M^{eff} = \frac{1}{i+1} \sum_{Q=j}^{Q=j+i} T_{M,q} \; . \tag{34}$$

المنارة للاستشارات
www.manaraa.com

A two-dimensional array of SD values against the regression T/T_M can be written as:

$$\sigma_{i,j}^2 = \frac{1}{i} \sum_{Q=j}^{Q=j+i} (T_q - \alpha - \beta \cdot T_{M,q})^2 . \tag{35}$$

The parameters of α and β, shown in Table D3, can be found from the linear regression.

Table D3. Parameters of α and β of the function $\sigma(T_M)$ for MTCS [30]

i	N_i	Estimation regression parameters	
		$\alpha_i, °C$	$\beta_i \cdot 10^{-3}, °C$
1	2	-0.64	6.6
2	3	-1.02	7.3
3	4	-0.97	7.3
4	5	-0.61	7.0
5	6	-1.06	7.5
6	7	-0.67	7.2
7	8	-0.01	6.6
8	9	-0.18	6.9
9	10	-0.28	7.2

A volume of the subsample, N_i is limited to a value of 19 due to a drastic increase of error for MTCS temperature measurements. The equation of SD as a function of time would be the following [30]:

$$\sigma(T_M) = -0.6 + 0.0071 \cdot T_M . \tag{36}$$

المنارة للاستشارات
www.manaraa.com

From the equation (36), it is obvious that a value of SD increases with a measured temperature rise for MTCS.

D.3 Measurement error estimation

As was discussed, a calibration function of the annealing temperature estimation measured with MTCS is a simple linear equation. The estimated parameters of the correlation function (tolerance limits) have to be applied to the entire measurement data including further measurements in order to estimate a truthfulness of the calibration function by means of a tolerance range for a measuring device. In this case, it is necessary to use a method of tolerance limits [33].

A value distribution of T_M (37) is expressed as a general equation for the limits of a tolerance range and can be written as (38) [30]:

$$\left(a + b \cdot T_{M,q} - T_q\right),\ q = 1,\ 2, ..., Q,\ \ Q = 18; \quad (37)$$

$$L^{(\pm)} = \pm(\alpha + \beta \cdot T_M) \cdot q_{\gamma,P,Ni}, \quad (38)$$

where $q_{\gamma,P,Q}$ is a coefficient of tolerance; N_i – is a volume of a subsample; subscript γ – is a confidence probability. Therefore [30]:

$$P = \left\{T^{ub} + L^{(-)} \leq T_{real} \leq T^{ub} + L^{(+)}\right\}, \quad (39)$$

where P – is a portion T_{real} values within the tolerance range; T – is an unbiased real temperature estimation. A value of q is obtained from the following equation [30]:

www.manaraa.com

Appendix D (Continued)

$$q_{\gamma,P,Q} = q_{\infty}(1 + \frac{x_{\gamma}}{\sqrt{2q}} + \frac{5x_{\gamma}^{2} + 10}{12q}), \quad (40)$$

where q_{∞} can be determined form the function (41) [30]:

$$2\Phi_{0}(q_{\infty}) = P, \quad (41)$$

and x_{γ} can be determined from the function (42) [30]:

$$\Phi_{0}(x_{\gamma}) = \gamma - 0.5, \quad (42)$$

$\Phi_{0}(x)$ - is a normalized Laplace's function (43) [30]

$$\Phi_{0}(x) = \frac{1}{\sqrt{2\pi}} \int_{0}^{x} e^{-u^{-3/2}} du. \quad (43)$$

Therefore, for $P = 0.95$, $\gamma = 0.9$, $Q = 18$, a coefficient of tolerance $q_{\gamma,P,Q} = 2.544$.
Then, from the equation (38), the limits of a tolerance range are:

$$L^{(\pm)} = \pm(-0.6 + 0.0071 \cdot T_{M}) \cdot 2.544, \text{ °C}. \quad (44)$$

Therefore, for a measured temperature range $600\,°C \le T_{M} \le 1200\,°C$, a tolerance range is:

$$9.4\,°C \le L^{(\pm)} \le 20.0\,°C. \quad (45)$$

المنارة للاستشارات
www.manaraa.com

D.4 Comparison of MTCS with other measurement techniques

In order to estimate how the MTCS method compares with other methods of temperature measurements in hard to access places, it is necessary to compare the σ (SD) values of the measurements as a function of time.

Techniques such as fusible plugs, thermal paints, thermoplugs and method of radioactive ^{85}Kr tracer are considered as the closest competitors to the MTCS among widely used non-contact readout methods [32, 22]. As for the method of fusible plugs and thermal paints method, the temperature measurements are obtained gradually. Using these methods it is possible to determine a temperature range for a uniform distribution of real temperature (46);

$$T_i^{\Delta} \leq T_{real} \leq T_{i+1}^{\Delta}, \quad (46)$$

where T_i^{Δ} - is a temperature of transient condition of an indicator (melting of plugs or a change of the color of thermal paints) for the lower temperature range; T_{i+1}^{Δ} - is the nearest temperature for the upper temperature range for the gauges, which remained in their initial condition.

The methods are characterized by three parameters: the number of stages in measurement, N; the range of measured temperature, $T_N^{\Delta} - T_1^{\Delta}$; and the uniformity of values for each stage. The σ value (SD) for each stage of measured temperatures for fusible plugs and thermal paints are determined using the condition of the uniform distribution of maximum temperatures. According to the method given by V. Kuznecov and V. Nikolaenko [30], the σ value is determined by a half of a range, divided by $\sqrt{3}$. For example, one of the two neighboring paints of the German thermal paint "Thermocolor" changes its color at 520 ˚C while the second – at 560 ˚C. A temperature range for this case is 40 ˚C. If the "520" paint changed its color during measurement,

المنارة للاستشارات
www.manaraa.com

and the “560” did not, then the σ would be:

$$\sigma = \frac{560 - 520}{2 \cdot \sqrt{3}} \approx 12\ °C\,. \tag{47}$$

The values of σ (SD) as a function of time, determined in the same manner for “Thermocolor” (Germany) and “Tempilac” thermal paints (USA) are shown in Figure D2; where 1 – diamond; 2 – 3C-SiC (MTCS); 3 – thermal paints “Tempilac” (USA); 4 – fusible plugs; 5 - thermal paints “Termocolor” (Germany); 6 – thermoplugs; 7 – ^{85}Kr tracers [30].

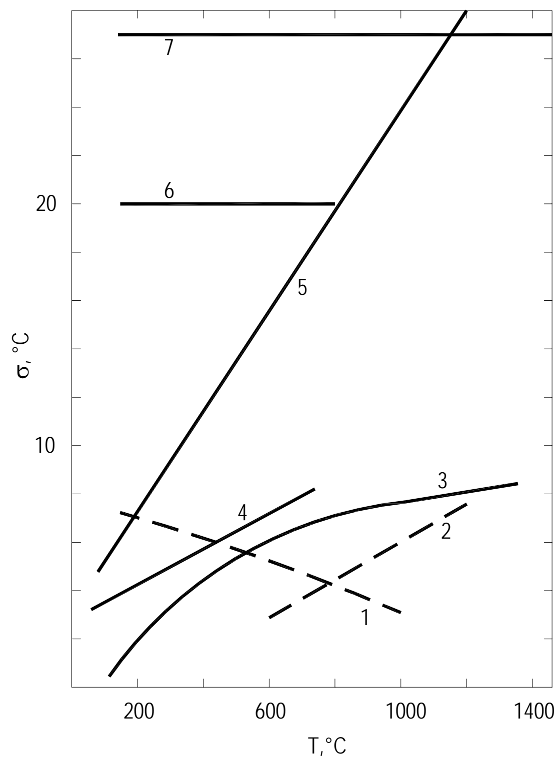

Figure D2. Standard deviation (σ) as a function of time

المنارة للاستشارات
www.manaraa.com

Below are the equations of σ (SD) for different measurements as a function of temperature [47]:

1. “Termocolor” thermal paints (Germany), N=30;

$40 \le T \le 1300$ °C ;

$\sigma(T) = 3.19 + 0.019554 \cdot T$.

2. “Tempilac” thermal paints (USA), N=83;

$100 \le T \le 1350$ °C ;

$\sigma(T) = -1.02 + 0.01713 \cdot T - 7.96 \cdot 10^{-6} \cdot T^2$.

3. Fusible plugs (USA), N=34;

$50 \le T \le 750$ °C ;

$\sigma(T) = 2.91 + 0.00707 \cdot T$.

Values of SD as a function of temperature T for fusible plugs, as well as the σ for MTCS and radioactive ^{85}Kr tracer are also shown in Figure D2. It is obvious that the method of MTCS gives the highest precision among the other methods used in hard accessible parts. The most accurate data for MTCS are achieved for the temperature range of 400 – 1200 ˚C. The closest to the MTCS method by the value of SD is the thermal paint “Thermocolor” method. However, the method of thermal paints has a considerable disadvantage that the paints may fall off the measured part during intensive gas flow or during vibrations, increasing the error of measurements.

المنارة للاستشارات

www.manaraa.com